

Penetration of Circular and Elliptical Liquid Jets into Gaseous Crossflow: A combined theoretical and numerical study

MASON MARZBALI

A Thesis

in

the Department

of

Mechanical and Industrial Engineering

Presented in Partial Fulfillment of the Requirements
for the Degree of Master of Applied Science (Mechanical Engineering) at
Concordia University
Montreal, Quebec, Canada

April 2011

©MASON MARZBALI, 2011

Concordia University
School of
Graduate Studies

This is to certify that the thesis prepared

By: **MASON MARZBALI**
Entitled: **Penetration of Circular and Elliptical Liquid Jets in Gaseous Crossflow: A combined theoretical and numerical study**

and submitted in partial fulfillment of the requirements for the degree of
Master of Applied Science (Mechanical Engineering)
Complies with the regulations of the University and meets the accepted standards with respect to originality and quality.

Signed by the final examining committee:

Dr. Muthukumaran Packirisamy Chair
Dr. Marius Paraschivoiu Examiner
Dr. Sam Li External
Dr. Ali Dolatabadi Supervisor

Approved by _____

MASc. Program Director,
Department of Mechanical and Industrial Engineering

April 2011 _____
Dean of Faculty

Abstract

PENETRATION OF CIRCULAR AND ELLIPTICAL LIQUID JETS IN GASEOUS CROSSFLOW:

A COMBINED THEORETICAL AND NUMERICAL STUDY

MASON MARZBALI

A combined theoretical and numerical study of liquid jet deformation discharged perpendicularly into a subsonic transverse gas flow is carried out. Near-field trajectory of the jet is determined from an analytical approach for momentum flux ratios up to 100. Force balance on liquid element is analyzed in free stream direction assuming that surface tension and viscous forces are small compared to the aerodynamic force acting on the liquid column. Mass shedding from jet surface and liquid evaporation are neglected; therefore, the jet cross-sectional area and the jet velocity are invariable. A logarithmic correlation for the trajectory of elliptical liquid jets is proposed that takes into account the liquid to gas momentum ratio and drag coefficient. The changes in freestream properties and the gas velocity are incorporated in terms of the drag coefficient. In the numerical part, the drag coefficients of elliptical profiles with various aspect ratios are formulated based on the gas *Reynolds* number using a two dimensional model. The trajectories of elliptical jets with various aspect ratios are calculated based on the obtained drag coefficients. It is shown that the jets with lower aspect ratios penetrate more into the crossflow. Furthermore, the deformation of a circular liquid jet subject to a gaseous crossflow is simulated using a three dimensional model. *Volume of Fluid* method is employed to capture the interface between the two phases and the first moment of closure is used to model *Reynolds* stresses in *Reynolds Averaged Navier-Stokes* equations. The deformations of the jet cross-section as the jet penetrates into the crossflow are illustrated. It is shown that the model is capable of resolving the *Counter-rotating Vortex Pair (CVP)* formed downstream of the jet.

Acknowledgements

I would like to express my best gratitude toward my academic advisor, Dr. Dolatabadi for his constant support and guidance during my master's program. The useful comments of Mr. Farvardin and Mr. Amini are greatly acknowledged. This work is partially supported by *Natural Sciences and Engineering Research Council of Canada (NSERC)* and *Le Fonds Québécois de la Recherche sur la Nature et les Technologies (FQRNT)*.

Table of Contents

List of figures.....	vii
List of tables	x
Nomenclature.....	xi
1 Introduction.....	1
1.1 Overview	1
1.2 Literature review	5
1.2.1 Liquid Jet injected to quiescent gas	5
1.2.2 Liquid jet in gas crossflow	11
1.3 Objectives.....	23
1.4 Thesis outline.....	24
2 Analytical approach.....	25
3 Numerical model.....	30
3.1 Volume of Fluid (VOF) method.....	31
3.2 Turbulence model	34
3.3 Solver and discretization schemes	38
3.4 Boundary conditions	39
3.4.1 2-D model.....	39
3.4.2 3-D model.....	40
4 Results and discussions	43

4.1	2-D numerical results	43
4.2	Analytical solutions.....	47
4.3	3-D numerical results	58
5	Closure.....	79
5.1	Conclusions	79
5.2	Recommendations for future work	81
6	Bibliography	82

List of figures

Figure 1-1: Schematic representation of the primary breakup regimes; (a) Rayleigh regime, (b) wind-induced regime, (c) atomization regime [3].	3
Figure 1-2: Breakup regimes map proposed by Ohnesorge and Miesse [2].	5
Figure 1-3: Stability curve of circular jet for different <i>Reynolds</i> numbers, (B) $Re_L=790$ ($We_G=0.06$), (C) $Re_L=5,500$ ($We_G=2.7$), (D) $Re_L=16,500$ ($We_G=24$), (E) $Re_L=28,000$ ($We_G=70$) [15].	9
Figure 1-4: Schematic of liquid jet breakup in gaseous crossflow [22].	12
Figure 1-5: Schematic of the vortical structures produced by a jet exhausted normally into a crossflow [41].	20
Figure 2-1: Schematic presentation of an elliptical liquid jet injected into a gaseous crossflow. .	26
Figure 3-1: Volume fraction representation in each cell containing both phases.	32
Figure 3-2: Piecewise Linear Interface Calculation (PLIC) representation of an interface.	33
Figure 3-3: Computational domain and boundary types for 2-D model.	39
Figure 3-4: Computational domain and boundary types for 3-D model.	41
Figure 4-1: Drag coefficient over half of an elliptical cylinder.	43
Figure 4-2: Drag coefficient plotted versus <i>Reynolds</i> number for a circular profile.	45
Figure 4-3: Drag coefficient plotted versus <i>Reynolds</i> number for aspect ratios of 0.5 and 0.25. .	46
Figure 4-4: Trajectory of water jet injected into air crossflow for momentum ratios equal to (a) 100, (b) 50, and (c) 10.	48
Figure 4-5: Effect of drag coefficient on the water jet trajectory; momentum ratios of (a) 100, (b) 50, and (c) 10 compared to experiments of Wu <i>et al.</i> [26].	49

Figure 4-6: Trajectory of water jet injected into air crossflow for two different <i>Weber</i> numbers and a constant momentum ratio of 18.	50
Figure 4-7: Jet trajectory for different liquids; momentum ratio of 50.	51
Figure 4-8: Jet trajectory for different liquids; momentum ratio of 18.	52
Figure 4-9: Penetration depth of a water jet in crossflow at elevated pressures and temperatures for momentum ratio of 50 compared to experiments of Ragucci <i>et al.</i> [30].	54
Figure 4-10: Trajectories of elliptical jets with various aspect ratios for momentum ratios of (a) 100, (b) 50, and (c) 10.	57
Figure 4-11: Liquid jet profiles for momentum ratios of (a) 100, (b) 50, and (c) 10.	58
Figure 4-12: Liquid jet cross-sections for momentum ratios of (a) 100, (b) 50, and (c) 10.	59
Figure 4-13: Pressure coefficient on the half-jet perimeter at four elevations for momentum ratio of 100.	60
Figure 4-14: Trajectories of a circular jet at momentum ratios of (a) 100, (b) 50, and (c) 10.	62
Figure 4-15: Contour of streamwise velocity for momentum ratio of 100 at (y/a): (a) 1, (b) 5, and (c) 10.	64
Figure 4-16: Contour of streamwise velocity for momentum ratio of 100 at (y/a): (a) 1, (b) 5, and (c) 10.	65
Figure 4-17: Contour of streamwise velocity for momentum ratio of 10 at (y/a): (a) 1, (b) 2, and (c) 8.	66
Figure 4-18: Contours of vertical velocity for momentum ratio of 100 at (y/a): (a) 1, (b) 5, and (c) 10.	68
Figure 4-19: Contours of vertical velocity for momentum ratio of 50 at (y/a): (a) 1, (b) 5, and (c) 10.	69

Figure 4-20: Contours of vertical velocity for momentum ratio of 10 at (y/a): (a) 1, (b) 2, and (c) 8.....	70
Figure 4-21: Contours of turbulent kinetic energy for momentum ratio of 100 at (y/a): (a) 1, (b) 5, and (c) 10.....	72
Figure 4-22: Contours of turbulent kinetic energy for momentum ratio of 50 at (y/a): (a) 1, (b) 5, and (c) 10.....	73
Figure 4-23: Contours of turbulent kinetic energy for momentum ratio of 10 at (y/a): (a) 1, (b) 2, and (c) 8.....	74
Figure 4-24: Streamlines for momentum ratio of 100 at (y/a): (a) 1, (b) 5, and (c) 10.	76
Figure 4-25: Streamlines for momentum ratio of 50 at (y/a): (a) 1, (b) 5, and (c) 10.	77
Figure 4-26: Streamlines for momentum ratio of 10 at (y/a): (a) 1, (b) 2, and (c) 8.	78

List of tables

Table 1-1: Energy budget in different jet breakup regimes [13].	7
Table 1-2: Jet breakup regimes and <i>Weber</i> number criteria.	10
Table 1-3: Disintegration regimes in crossflow [23].	13
Table 1-4: Summary of test conditions for liquid jet injected into gas crossflow.	19

Nomenclature

a	=	semi-major axis of an ellipse
AR	=	aspect ratio (b/a)
b	=	semi-minor axis of an ellipse
C_D	=	drag coefficient
D_0	=	jet diameter
$D_{eq.}$	=	equivalent diameter ($2\sqrt{ab}$)
D_H	=	channel hydraulic diameter
n	=	normal direction
Oh	=	Ohnesorge number ($\mu_j / (\rho_j D_0 \sigma)^{1/2}$)
q	=	liquid to gas momentum flux ratio ($\rho_j V_j^2 / \rho_\infty U_\infty^2$)
Re	=	free stream <i>Reynolds</i> number ($\rho_\infty U_\infty D_{eq.} / \mu_\infty$)
Re_j	=	jet <i>Reynolds</i> number ($\rho_j V_j D_0 / \mu_j$)
Re_{ch}	=	channel <i>Reynolds</i> number ($\rho_\infty U_\infty D_H / \mu_\infty$)
p	=	pressure
s	=	streamwise direction
T	=	temperature
u	=	x -velocity
v	=	y -velocity
w	=	z -velocity
We	=	free stream <i>Weber</i> number ($\rho_\infty U_\infty^2 D_{eq.} / \sigma$)
We_{aero}	=	aero <i>Weber</i> number ($\rho_\infty V_j^2 D_0 / \sigma$)
x	=	free stream direction
y	=	vertical direction
z	=	spanwise direction

Greek letters:

σ	=	surface tension
δ	=	thickness, Dirac delta function
μ	=	viscosity
θ	=	deflection angle
ρ	=	density

Subscripts:

0	=	initial property
f	=	friction
g	=	gas property
l	=	liquid property
j	=	jet property
∞	=	crossflow property

1 Introduction

This chapter includes a brief overview of liquid jet breakup and atomization. The most relevant literature in liquid jet breakup is reported herein.

1.1 Overview

Atomizers are widely used in various industrial applications such as coating, spray cooling, combustion engines, and pharmaceutical industries. Among all types of atomizers plain orifices have been widely utilized owing to their simplicity and ease of manufacturing. These orifices are capable of emerging different shapes of jet depending on their internal geometry with most common type being circular jets which have been studied for more than a century; however, there remain a lot of unknowns that need to be investigated. Another shape that recently absorbed attention of researchers is elliptical orifice. Since the free surface of a liquid jet always seeks configurations with minimum surface energy, elliptical jets require less energy to breakup due to the inherent instabilities. Besides, surface area of elliptical jet is larger than its circular counterpart with the same equivalent diameter, hence it disintegrates faster and an increase in orifice aspect ratio causes further destabilization of elliptical liquid jets. The benefit of such orifices is smaller breakup length and producing finer droplets at the end of atomization process.

One of the interesting phenomena about elliptical jets that have been studied by researchers such as Kasayep and his coworkers [1] is axis-switching of the jet column. At sufficiently high *Weber* number the jet dilutes in one of its axes and contracts in the other direction and this will repeat periodically until it breaks up. The axis switching phenomenon is analogous to oscillation of a spring-mass system. The amplitude of disturbance overshoots several times until it becomes over

critical and rupture happens. Onset of axis-switching process results in a significant reduction of the breakup length. Kasayep *et al.* [1] used different aspect ratios for elliptical orifices and two liquid types, viz., water and water/glycerol mixture. The viscosity of the liquid plays an important role in the process of breakup. They found out that for flow conditions with low *Weber* and *Reynolds* numbers absence of axis-switching causes elliptical jets to behave in a similar manner to that of equivalent circular jet. By increasing the liquid *Weber* number the breakup length first increases until it reaches a maximum and drops rapidly after this point. An increase in nozzle aspect ratio results in shortening the length of breakup and presence of viscosity damps axis-switching process.

The breakup of liquid jets consists of two main mechanisms; Primary and secondary breakup. At the primary stage, an elliptical liquid jet will breakup faster compared to circular jet with the same cross sectional area. This is beneficiary if employed in cross flow, because less momentum exchange between liquid and gas is required to carry out the breakup. The drawback though is manufacturing of such holes and when we aim at smaller diameters it is even more challenging.

The mechanisms of liquid breakup are not well understood yet, however, many different sources have been reported to contribute to the primary breakup of jets; most common factors are [2],

- Velocity profile at the nozzle exit
- Cavitations inside the nozzle
- Turbulent flow inside the nozzle and at the exit
- Nozzle internal geometry such as length to diameter ratio
- Ambient pressure

The latter amplifies instabilities generated on the jet surface (Kelvin-Helmholtz instability). The type of instability depends on relative values of forces acting on the fluid. Commonly considered

driving forces are: surface tension, aerodynamic shear, air turbulence and viscous stratification. Hydrodynamic instabilities are expected to be at the root of liquid jet breakup and are generally divided into three distinct categories.

1. *Rayleigh*: this mechanism is responsible for breakdown of ligaments on sheets and films for many operating conditions.
2. *Kelvin-Helmholtz*: these instabilities are driven by aerodynamic shear.
3. *Tollmein-Schlichting*: which are due to effect of gas-phase turbulence.

The difference between breakup mechanisms is schematically presented in figure 1-1.

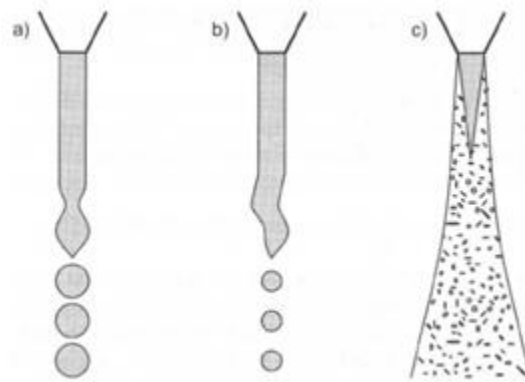


Figure 1-1: Schematic representation of the primary breakup regimes; (a) Rayleigh regime, (b) wind-induced regime, (c) atomization regime [3].

Hydrodynamic instability theories predict the most unstable wavelength as the one with the fastest growth rate and suggest that this wavelength dominates the other wavelengths and the droplet size is proportional to it [4]. It is believed that the breakup happens when the disturbances grow to a point where the interface contacts itself. However, the theory that atomization is due to aerodynamic interaction between two phases which leads to unstable wave growth has not found universal acceptance [2]. In fact, Reitz and Bracco [5] concluded that no single mechanism is responsible for jet breakup and often a combination of factors is involved.

The liquid jet breakup is normally triggered by interaction between two fluids with different densities and velocities. At low *Weber* numbers breakup is a result of long-wavelength disturbances growing on liquid surface whereas at high *Weber* numbers short-wavelength disturbances. Droplets pinched off from end of the jet are the same order of magnitude compared to jet diameter in Rayleigh and first wind-induced regime. Whereas in second wind-induced and atomization regime droplets are stripped off from liquid surface with much smaller diameters than that of the jet. Lightfoot [6] has recently reviewed the breakup regimes and disturbance breakdown categories in quiescent gas, the reader is referred to [6] for more details.

1.2 Literature review

1.2.1 Liquid Jet injected to quiescent gas

The very first fundamental study of liquid jet breakup has started by Rayleigh [7] more than 100 years ago. He analyzed non-viscous jets in laminar regime and reported the root of jet breakup as hydrodynamic instabilities. A few decades later Weber [8] found the effect of liquid viscosity and gas density on liquid jet breakup. Taylor [9] was among those who also studied the effect of gas density. Until 1978 when Reitz [10] added gas to liquid density ratio as third abscissa to jet breakup regime chart originally developed by Miesse [11] and Ohnesorge [12] who plotted Ohnesorge number versus *Reynolds* number dividing breakup regime to three distinguishable categories; Rayleigh, Wind Induced, and Atomization regimes as shown in figure 1-2. A review of previous works on liquid jet disintegration has been done by Lefebvre and can be found in [2].

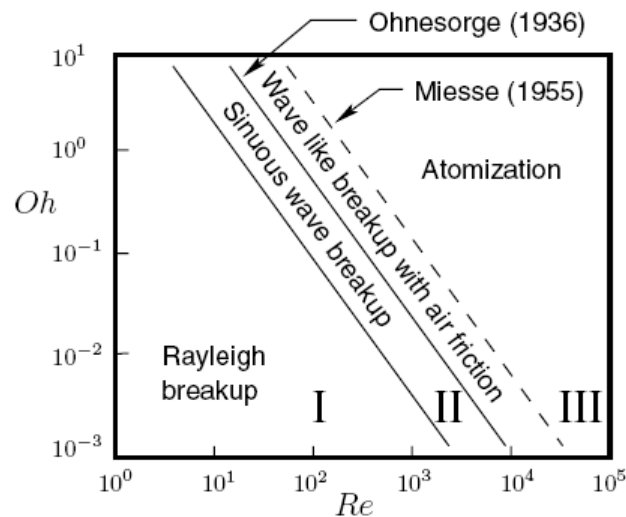


Figure 1-2: Breakup regimes map proposed by Ohnesorge and Miesse [2].

Breakup regimes after Reitz [3] are generally categorized into five well known classifications.

1. *Dripping regime*: at very low jet velocities, bulks of fluid are disintegrated from liquid jet and capillary force dominates the breakup.
2. *Rayleigh breakup regime*: in this regime instabilities are purely driven by surface tension forces and produced droplets sizes are larger than the jet diameter. There is a balance between liquid inertia and surface tension and the jet surface is unstable.
3. *First wind induced*: in this regime aerodynamic effects are important and enhance disturbance growth and may alter the instabilities. Droplet size is the same order as jet diameter and surface tension forces start to oppose the breakup.
4. *Second wind induced*: in this regime aerodynamic effects dominate surface tension effects and large numbers of small disturbances propagate at the surface of the jet. These disturbances are enhanced due to the relative velocity between liquid and gas which eventually break up the jet into small droplets with a size smaller than jet diameter. By further increase in gas inertia, the unstable growth of surface waves with short wavelengths causes the jet breakup.
5. *Atomization*: in atomization regime the jet disintegrates immediately after exiting the nozzle with no observable intact length. The atomization is not actually instantaneous but some intact length exists on which disturbances quickly form, grow and break down. Produced droplet sizes are much smaller than jet diameter. It usually happens at high *Weber* numbers and breakup starts at nozzle exit and the spray is conical.

Lin and Reitz [13] have tabulated the mechanical energy budget of liquid jet calculated from the Navier-Stokes equations by Lin and Creighton [14]. They expressed the sum of the rate of work

done by various relevant forces over a wavelength of the most amplified disturbance in a controlled volume of the jet as follows.

$$E = P_g + P_l + S + V + D \quad (1-1)$$

where P_g is the rate of work done by the gas pressure fluctuation at the liquid-gas interface, P_l is the rate of work done by the liquid pressure fluctuation at the inlet and outlet of the control volume, S is the rate of work done by the surface tension, V is the rate of work done by the liquid viscous stress, and D is the rate of viscous dissipation of mechanical energy. Table 1-1 shows the energy budget breakdown for different *Reynolds* and *Weber* numbers. Q is gas to liquid density ratio and the value of 0.0013 corresponds to the case of a water jet in air under atmospheric condition. k_r ($k_r = 2\pi a / \lambda_m$) is wave number of the most amplified disturbance predicted by the linear theory for the flow parameters specified in the first three columns.

Re_L	$10^3/We_L$	$Q \times 10^3$	k_r	s	p_g	p_ℓ	v	d
2	1.25	1.3	0.1669	117.5	3.5	-0.2	0.2	-21.6
102	1.25	1.3	0.5725	97.7	26.2	-4.9	1.6	-20.6
4×10^2	2.50	1.3	0.7701	65.5	41.8	0.0	0.1	-7.4
4×10^4	1.25	0.1	0.7088	96.2	3.5	0.4	0.0	-0.1
11016	0.882(-2)	1.3	35.417	-296.0	547.7	-2.1	-0.1	-149.5
36720	0.882(-2)	1.3	40.051	-215.1	351.7	-2.0	0.1	-34.7
67411	0.882(-2)	1.3	41.580	-210.4	331.6	-1.9	0.0	-19.3
116122	0.802(-2)	1.3	42.368	-214.7	332.1	-1.0	-0.2	-16.2

Table 1-1: Energy budget in different jet breakup regimes [13].

Four different categories are distinguished in the above table.

1. *Capillary pinching*: at very low *Reynolds* numbers Rayleigh predicted the wavelength of the most unstable disturbance for non-viscous jets to be greater than jet circumference. If the wavelength of disturbance is smaller than the minimum wavelength ($\lambda_{\min} = \pi D_0$) then

it will be damped by restoring force i.e. surface tension. On the other hand, the instabilities with wavelengths greater than λ_{\min} will be amplified and the one with the optimum wavelength (λ_{opt}) controls the breakup. Rayleigh proposed a λ_{opt} equal to $4.51D_0$ resulting in droplet size of $1.89D_0$. However, *Weber* took into account the viscosity of the jet and proposed λ_{opt} as,

$$\lambda_{opt} = \sqrt{2\pi}D_0(1+3Oh)^{0.5} \quad (1-2)$$

2. *Rayleigh breakup regime*: by increasing *Reynolds* number at row 2 we find out the work done by gas pressure fluctuation comes into play as liquid-gas relative velocity has been increased which assists surface tension force. The droplets are predicted to have a size in same order of jet diameter.
3. *First wind-induced regime*: in row 3 and 4 the breakup is dominated by surface tension force and gas inertia is still in favor of capillary forces.
4. *Second wind-induced and the atomization regimes*: in the last four rows we can see surface tension counteracts inertia; hence, the pressure work has to be higher to dominate surface tension in the formation of droplets. Smaller drops are expected in these regimes since the wave number is increased one order of magnitude.

The stability curve for a cylindrical jet and the location of the last four breakup regimes with their corresponding visualizations is illustrated in figure 1-3. The breakup length, defined as the length of intact liquid core, increases with liquid velocity lower than U_{LC} which is the onset of first wind induced regime. In Rayleigh mode the jet breakup length for a known fluid type and same nozzle diameter, hence constant Ohnesorge number, is characterized by *Weber* number based on liquid properties. As aerodynamic forces come to the play at higher jet velocities a *Weber* number based on gas properties and liquid-gas relative velocity is defined to take the gas

effects into consideration. Table 1-2 summarizes the criteria corresponding to all of the atomization regimes.

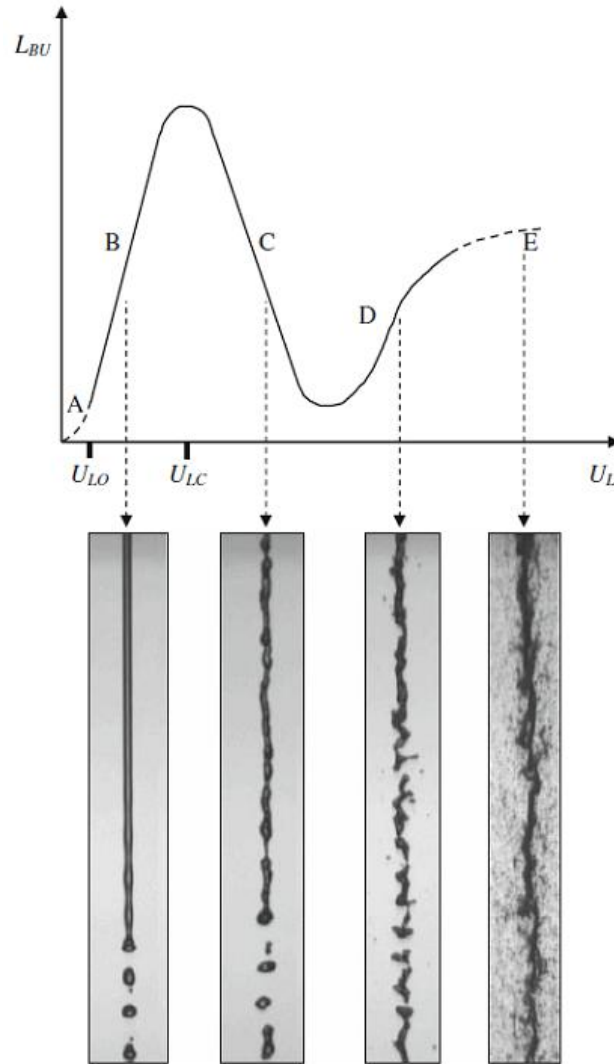


Figure 1-3: Stability curve of circular jet for different *Reynolds* numbers, (B) $Re_L=790$ ($We_G=0.06$), (C) $Re_L=5,500$ ($We_G=2.7$), (D) $Re_L=16,500$ ($We_G=24$), (E) $Re_L=28,000$ ($We_G=70$) [15].

Disintegration regime	Weber number Criteria	Mode of breakup
Dripping	$We_L < 8$ [16]	Capillary
Rayleigh	$We_L > 8, We_G < 0.4$ [16]	Bulk fluid
First wind induced	$1.2 + 3.41 Oh^{0.9} < We_G < 13$ [16], [17]	Bulk fluid
Second wind induced	$13 < We_G < 40.3$ [11]	Surface
Atomization (Spray)	$We_G > 40.3$ [11]	Surface

Table 1-2: Jet breakup regimes and Weber number criteria.

Stiesch [18] reported that liquid inertia force is dominant on surface tension in Rayleigh breakup regime and oscillations result in droplets greater than the nozzle diameter. At moderate Weber numbers inertia of gas phase becomes more important and disturbances are triggered by liquid gas interactions which grow up until breakup and droplet diameter is in the range of nozzle diameter. By increasing the liquid-gas relative velocity, aerodynamic forces are intensified and wavelengths of disturbances become shorter, therefore, the breakup length decreases. At high Weber numbers two breakup lengths can be identified; surface breakup starting at nozzle orifice and intact core several nozzle diameters downstream of the orifice with a conical shape. The mean droplet diameters are much smaller than the nozzle diameter; hence, this regime is of importance for high pressure atomizers. Reitz [10] reported that atomization of injected liquid and the subsequent of breakup of drops are indistinguishable processes within a dense spray. The liquid jet is more stable at higher Ohnesorge numbers (higher viscosity and lower surface tension) and needs larger initial disturbance to bring about instability [19].

1.2.2 Liquid jet in gas crossflow

Disintegration and atomization of liquid jet column discharged into crossflowing gas has found its way through many industrial applications such as gas turbine engines, rocket engines, film cooling, coating [20]. Many parameters are found to be influential in such a process; jet to crossflow momentum flux ratio, injection angle, jet exit geometry, jet velocity profile, and crossflow turbulence.

Consider a jet of liquid emerging out of the nozzle orifice as schematically shown in figure 1-4. The liquid jet is deflected by the drag force exerted by the gas on liquid column; the distribution of static pressure around jet surface while gas flow accelerates over the liquid column causes a deformation of its cross section [21]. This results in stretching of the jet normal to gas flow direction until part of liquid column is detached from its core, e.g. in bulk, ligament or droplet form, depending on crossflow parameters. Disintegration of liquid jet occurs predominantly by two different mechanisms which are known as surface breakup mechanism and column breakup mechanism. The surface breakup mechanism is characterized by the gradual erosion of the jet, as droplets are stripped off from the sides of the liquid jet by the shearing action of the crossflow. The column breakup mechanism, on the other hand, is initiated by the growth of waves on the surface of the jet and possibly also of instabilities within the jet. Ultimately, jet fracture occurs in a trough of a wave, giving rise to the formation of ligaments and clusters of fragments.

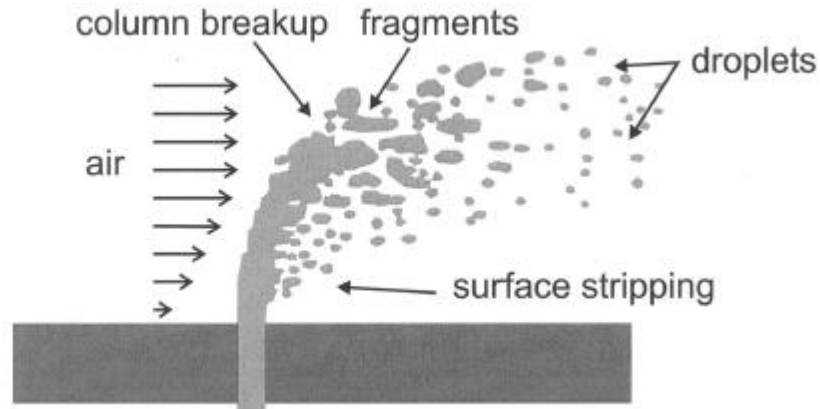


Figure 1-4: Schematic of liquid jet breakup in gaseous crossflow [22].

The products of primary atomization according to the column breakup mechanism are subsequently subjected to secondary atomization. If aerodynamic pressure is high, then shear breakup mechanism is dominant of both jet surface and secondary atomization.

The generally accepted classification of a jet breakup in crossflow is as follows.

1. *Column breakup*: it happens when the aerodynamic forces (drag and lift) are higher than viscous and surface tension forces. Aerodynamic forces enhance the breakup of the jet into smaller liquid portions, i.e. bulk, ligament or droplet. Detached parts are in the order of the jet diameter, and large scale disturbances caused by hydrodynamic instabilities are at the root of the breakup. Hence, this mode is analogous to bulk fluid mode.
2. *Bag breakup*: the jet is stretched into a thin sheet bounded by two rims when the liquid entrains air into a pocket causing it to grow. Eventually, the air pressure inside the bag causes the pocket to catastrophically fail producing small droplets and a thick rim. This rim ruptures downstream via Rayleigh mechanism and two droplet sizes are produced; one from ruptured membrane and one from ligaments bounding the membrane.

3. *Multi-mode regime*: a transitional regime where a part of the jet remains intact and rest of the jet breaks up due to surface mode.
4. *Shear mode*: the jet column deforms and ligaments and droplets are stripped from its surface. Hence, this mode is analogous to the second wind induced regime.

Table 1-3 includes the *Weber* criteria based on the gas velocity for each category.

Disintegration regime	Criteria	Mode of breakup
Column	$We < 4$	Bulk fluid
Bag	$4 < We < 30$	Mixed
Multi-mode	$30 < We < 100$	Mixed
shear	$We > 100$	Surface

Table 1-3: Disintegration regimes in crossflow [23].

Numerous studies have been done with applications in engineering problems, e.g. combustion, where secondary breakup of droplets and their size distribution are of importance. In these cases, a gas flow with relatively high speed strips off the drops from the jet surface, thus, the rate of mass shedding depends on the test conditions and type of fluid being used. Therefore, a distinct leeward profile is not recognizable. On the other hand, there are some applications, e.g. spray coating, where higher jet penetration is desirable. Hence, liquid column bending and its primary breakup become of importance.

One of the most important characteristics of a liquid jet in a crossflowing gas is the spray trajectory. Most experimental studies focus on this aspect and different correlations are suggested by many researchers in forms of power-law, hyperbolic, exponential, and logarithmic

functions depending on their type of analysis and test conditions. Some of the most recent correlations found in literature are reported herein.

Vich and Ledoux [24] proposed a hyperbolic expression for jet trajectory in crossflow as the following using a simple analytical model.

$$y(x) = \frac{\pi}{2C_D} q \left[\cosh \left(\frac{2C_D}{\pi} \frac{x}{q} \right) - 1 \right] + y'_0 x \quad (1-3)$$

where C_D and q are the drag coefficient and momentum ratio, respectively. y'_0 is the initial slope of the jet trajectory and it's zero for perpendicularly injected jet.

Numerous correlations indicate a power-law trajectory in the following general form,

$$\frac{y}{D_0} = A q^B \left(\frac{x}{D_0} \right)^C \quad (1-4)$$

where constants A , B and C are determined from regression of the results. D_0 indicates the initial diameter of the jet.

Wu *et al.* [25] experimentally and theoretically studied trajectories of liquid jets injected into subsonic air crossflow at standard conditions using PDPA and shadowgraph techniques [26]. They conducted experiments for water, alcohol/water and glycerol/water mixtures for momentum ratios ranging from 5.3 up to 48.8, crossflow *Weber* between 55 and 647, jet *Weber* from 1.15 to 20.3. They identified two breakup modes as the column breakup and shear breakup for momentum ratios between 5-100 and *Weber* from 80 to 800. They found the borderline of the transition between column and surface breakup.

$$\log(We_{crit.}) = [3.1 - \log(q)] / 0.81 \quad (1-5)$$

They developed trajectory correlations by force analysis and suggested the following correlation for column breakup regime.

$$\frac{y}{D_0} = \sqrt{\frac{\pi}{C_D} q \left(\frac{x}{D_0} \right)} \quad (1-6)$$

where C_D is equal to 1.696 for water and for other liquids they established the following empirical correlation.

$$\frac{C_D}{C_{D_{Water}}} = 0.984 \left(\frac{\mu_j}{\mu_{Water}} \right)^{0.364} \quad (1-7)$$

In addition, they proposed an additional correlation for droplet regime.

$$\frac{y}{D_0} = 4.3q^{0.33} \left(\frac{x}{D_0} \right)^{0.33} \quad (1-8)$$

Hassa and Beckerand [27] suggested a logarithmic correlation by investigating the breakup, penetration, and atomization of a plain jet of Kerosene A-1 fuel in a non-swirling crossflow of air at gas turbine conditions. They suggested near-field penetration for momentum flux ratios between 1 and 40, gas *Weber* number from 90 to 2120, and axial location from 2 up to 22 jet diameters as the following correlation.

$$\frac{y}{D_0} = 1.48q^{0.42} \cdot \ln \left\{ 1 + 3.56 \frac{x}{D_0} \right\} \quad (1-9)$$

Moreover, for the lateral dispersion for momentum ratios between 1-26, *Weber* of 360 up to 2120, and axial location from 2 to 18 jet diameters they proposed equation (1-10).

$$\frac{z}{D_0} = 2.32q^{0.09} \left(\frac{x}{D_0} \right)^{0.32} \quad (1-10)$$

Tambe [28] has also reported a logarithmic correlation by studying the jet and spray characteristics in subsonic crossflow under atmospheric conditions for three liquid types; Water, Jet A-1, and N-Heptane as equation (1-11).

$$\frac{y}{D_0} = 1.55q^{0.53} \cdot \ln \left\{ 1 + 1.66 \frac{x}{D_0} \right\} \quad (1-11)$$

One of the recent correlations that contain both liquid viscosity and gas *Weber* number was proposed by Stenzler *et al.* [29]. They obtained Mie scattering images for momentum flux ratios of 9, 14, and 18 for Water, acetone, and 4-Heptanone, then, suggested a power-law correlation in a general form as follows.

$$\frac{y}{D_0} = Aq^B \left(\frac{x}{D_0} \right)^C We^D \left(\frac{\mu_j}{\mu_{H_2O}} \right)^E \quad (1-12)$$

A, *B*, *C*, *D* and *E* are coefficients obtained from least squares regression method at increments of 20 jet diameters. They concluded that when *D* and *E* are set to zero, a correlation based on momentum flux ratio similar to conventional correlations is obtained. In fact these coefficients have to be negative to account for decrease of penetration depth when gas *Weber* number or liquid viscosity is increased.

After them, Ragucci *et al.* [30] have experimentally investigated liquid jets in crossflow at both elevated pressure and temperature. They tested water and Jet A-1 fuel at pressures up to 2 MPa and temperatures up to 600 K. Their correlation includes the gas viscosity and aero *Weber* number which is calculated based on gas properties and the liquid velocity.

$$\frac{y}{D_0} = 2.28 q^{0.422} We_{aero}^{-0.015} \left(\frac{\mu}{\mu_{air,300K}} \right)^{0.186} \left(\frac{x}{D_0} \right)^{0.367} \quad (1-13)$$

Furthermore, Amighi *et al.* [31] reported a correlation using both liquid and gas *Reynolds* numbers based on the jet equivalent diameter and channel hydraulic diameter, respectively. They obtained experimental results on the penetration of a water jet exhausted into air crossflow under atmospheric and elevated pressures and temperatures. In their study, liquid to air momentum ratios varied from 10 to 80. Air temperatures of 25, 200, 300°C and absolute crossflow air

pressures of 30, 55, 75 psia have been used. They employed pulsed laser sheet illumination technique and concluded that liquid jet velocity has a greater effect on spray trajectory than the crossflow velocity. For centerline trajectory they proposed a correlation obtained from regression analysis of time-averaged and filtered images as follows.

$$\frac{y}{D_0} = 0.191 \left(\frac{x}{D_0} \right)^{0.43} q^{0.30} \text{Re}_{ch}^{0.12} \text{Re}_j^{0.14} \quad (1-14)$$

In order to calculate the *Reynolds* numbers in the above correlations, the crossflow air viscosity was obtained at the crossflow air temperature while the liquid viscosity and surface tension were calculated at the film temperature (average of the liquid temperature and the crossflow air temperature).

In a recent study, Mashayek *et al.* [32] developed a theoretical model for deformation of circular liquid column to elliptic shape. They obtained a nonlinear equation for deformation of jet cross-sectional element by balancing aerodynamic, viscous, and surface tension forces employing the analogy between an oscillating two-dimensional drop and a forced mass-spring system. They calculated the drag coefficient on circular and elliptical liquid columns with different aspect ratios for various *Reynolds* numbers using a 2-D transient model. They interpolated for a range of *Reynolds* numbers between 150 and 8000 and proposed the following correlations.

$$\text{AR}=1: C_D = (-3.46 \times 10^{-12}) \text{Re}^3 + (5.22 \times 10^{-8}) \text{Re}^2 - (2.01 \times 10^{-4}) \text{Re} + 1.0 \quad (1-15)$$

$$\text{AR}=2: C_D = (3.83 \times 10^{-15}) \text{Re}^4 - (7.37 \times 10^{-11}) \text{Re}^3 - (4.66 \times 10^{-7}) \text{Re}^2 - (9.62 \times 10^{-4}) \text{Re} + 1.7 \quad (1-16)$$

$$\text{AR}=4: C_D = 6.22 \text{Re}^{-0.1949} \quad (1-17)$$

$$\text{AR}>10: C_D = 1.98 \quad (1-18)$$

They found out that mass stripping from jet column has a great influence on its trajectory in crossflow at *Weber* numbers higher than 60 based on Mazallon *et al.* [23]. They concluded that neglecting mass reduction leads to over prediction of jet deflection and drag force (due to the excess mass). In another work, Sivakumar *et al.* [33] studied the variations of drag coefficient for aspect ratios of 0.2 up to 5 for Newtonian and non-Newtonian fluids with power law index ranging from 0.2 to 1.8 at *Reynolds* numbers between 0.01 and 40. They used steady, laminar 2-D model with unstructured quadrilateral cells of non-uniform spacing for their simulations. They proposed correlations for drag coefficient based on power-law index, elliptical aspect ratio, and *Reynolds* number. Since the *Reynolds* number was limited to 40 in their study, their correlations are not used in this work.

Ryan [34] proposed a novel numerical method composed of two separate sub-models. The gas crossflow was simulated via CFX commercial code to predict local pressure and velocity of gas around deflected liquid column. On the other hand, the liquid jet deformation was implemented using *Volume of Fluid* model linked to CFX using an iterative procedure. Time-averaged trajectories in their range of interest showed consistency with experimental data.

Table 1-4 summarizes all the test conditions in the aforementioned works. The broad difference between empirical correlations could be the result of the analysis and regression type, different test conditions, experimental uncertainties, etc. All the empirical correlations are power-law functions except for Hassa [27] and Tembe [28] which are logarithmic. The correlation of Stenzler *et al.* [29] includes the effect of liquid viscosity and the freestream *Weber* number. On the other hand, the correlation of Ragucci *et al.* [30] uses the gas viscosity and the aero *Weber* number based on the jet velocity. In the most recent study, Amighi *et al.* [31] incorporated liquid and gas *Reynolds* numbers into their correlation.

Author(s)	Liquid type	D_0 (mm)	V_j (m/s)	U_∞ (m/s)	Momentum ratio	Analysis type	Pressure and temperature
Vich and Ledoux [24]	Water	0.5, 1.0, 1.5	0-30	0-40	N/A	Back-lighted photography	Atmospheric
Inamura <i>et al.</i> [35]	Water, Aluminum suspension	0.5, 1.0, 2.0	7-26	55-140	2.5- 225	Back-lighted photography	Atmospheric
Wu <i>et al.</i> [25], [26]	Water, Ethyl Alcohol, Alcohol/water, Glycerol/water	0.5, 1.0, 2.0	8.9-37.7	68.1-141	3.3-185	Pulsed shadowgraph, PDPA	Atmospheric
Hassa and Becker [27]	Jet- A1	0.45	N/A	50-100	2-18	Shadowgraph, Mie scattering, PDA	Elevated
Tambe [28]	Water, Jet-A1, N-Heptane	0.38, 0.76	3-26	89-215	0.7-10.2	Pulsed shadowgraph, PDPA	Atmospheric
Cavaliere <i>et al.</i> [36]	Water, Jet-A1	0.3, 0.5	10-55	20-55	5-280	Numerical model	Elevated
Madabhushi [37]	Water	0.5	12.8-42.5	68.7- 137	9- 48.8	Numerical model	Atmospheric
Ryan [34]	Water	0.5	N/A	N/A	158	Numerical model	Atmospheric
Lin <i>et al.</i> [20]	Water, Ethyl alcohol, Alcohol/water	0.5- 2.0	N/A	69-137	2-40	Shadowgraph, PDA	Elevated
Ng <i>et al.</i> [38]	Water, Ethyl Alcohol	0.5, 1.0, 2.0	7- 50	10-60	9- 1199	Pulsed shadowgraph, high speed imaging	Atmospheric
Mazallon <i>et al.</i> [23]	Water, Ethyl Alcohol, Glycerol	1.0	N/A	N/A	100- 8000	Pulsed shadowgraph	Atmospheric
Stenzler <i>et al.</i> [29]	Water, Acetone, 4-Heptanone	0.29	1.3-16.3	10.8-118.7	9, 14, 18	Mie scattering, PDPA	Atmospheric, elevated
Amighi <i>et al.</i> [31]	Water	0.4, 0.5	6.8-54	22-156	10-80	Pulsed laser sheet illumination	Atmospheric, elevated
Mashayek <i>et al.</i> [32]	Water, Acetone, Ethyl alcohol, Glycerol, etc.	0.45, 0.5	20	75-100	2-72	Theoretical model	Atmospheric, elevated

Table 1-4: Summary of test conditions for liquid jet injected into gas crossflow.

In addition to the spray trajectory the main features of liquid jets in a crossflow are associated with four distinct vortices which are generated by the interaction between jet exit shear layer and crossflow boundary layer as reported in [39], [40]. These vortices are schematically illustrated in figure 1-5 reproduced from New *et al.* [41] and described below.

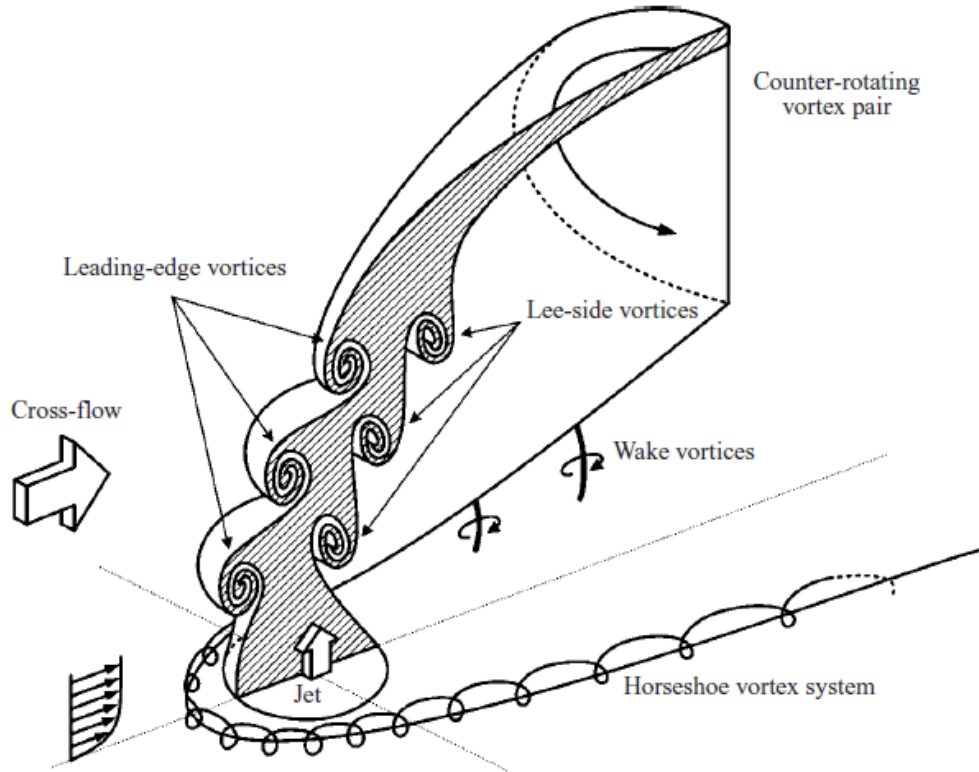


Figure 1-5: Schematic of the vortical structures produced by a jet exhausted normally into a crossflow [41].

1. *Horseshoe vortex:* it is similar to horseshoe vortex created upstream of a solid bluff body in transverse flow. It is generated by the accumulation of crossflow boundary layer vorticity at the stagnation point upstream of jet.
2. *Jet shear layer vortices:* these vortices also known as rollups appear at the wind side of jet and originate from Kelvin-Helmholtz instabilities.

3. *Counter-rotating vortex pair (CVP)*: as shear layer vortices are convected downstream they cancel out the upstream vortices which are rotating in the opposite direction and superposition of all these vortices downstream of the jet creates a vortex pair, so called *Counter-rotating Vortex Pair (CVP)*. This vortex pair is known to be the most dominant compared to other vortices and has been exclusively studied in [42].
4. *Wake vortices*: Fric [39] argued that some segments of the horseshoe vortex which wraps around the jet will be detached on the lee side and are carried upward with the jet flow and eventually shed vortices in the wake region behind the jet. Conversely, Morton [43] stated that wake vortices are not similar to vortex shedding behind bluff bodies.

Morton [43] proved that in a constant-density incompressible flow vorticity can only be generated at solid boundaries by the pressure gradients acting tangentially along the wall. Numerical simulation of all these vortex types is a challenging task and it requires a rigorous turbulence model which is usually computationally very expensive. There is no universally accepted turbulence model for this class of problem as many authors issued contradictory statements. For instance, Alvarez *et al.* [44] have employed first and second moment closure to model *Reynolds* stresses and concluded that overall performance of both models in comparison to measured data are similar but for higher velocity ratios *Reynolds Stress Model (RSM)* offers better agreement over $k-\varepsilon$. Dai *et al.* [45] have examined *Standard* and *Realizable $k-\varepsilon$, Reynolds stress Model (RSM)*, and *Spalart-Allmaras* turbulence models with two wall treatments; nonequilibrium wall function and enhanced wall treatment. They reported that *RSM* does not show any advantage over *Realizable $k-\varepsilon$* whereas other studies [46], [47] confirmed that $k-\varepsilon$ fails to predict the horseshoe vortex observed in experiments and it is not tuned for such an application. Savory *et al.* [48] reported that $k-\varepsilon$ is not capable of reproducing the

vorticity diffusion further downstream of the nozzle and overpredicts a circulation about 50% whereas *RSM* along with quick differencing shows better agreement compared to measurements. Hoda and Acharya [49] investigated the performance of seven turbulence models; high *Reynolds* $k-\varepsilon$ model of Launder and Spalding [50], low *Reynolds* $k-\varepsilon$ of Launder–Sharma [51] and Lam–Bremhorst [52], low *Reynolds* $k-\omega$ model of Wilcox and Traci [53], *DNS*-Based Low-*Re* $k-\varepsilon$ model of Rodi and Mansour [54], Nonlinear Low-*Re* Models of Mayong and Kasagi [55], and Speziale [56]. They compared their numerical results against experimental data of Ajersch *et al.* [57] for velocity ratio of 0.5 at *Reynolds* number equal to 4700. They concluded that all of them are somehow insufficient for such a complex flow because not all the main flow features are captured properly by these turbulence models due to certain shortcomings and in some cases the turbulence levels are overpredicted. In most cases the wake vortices and horseshoe vortex are not resolved.

Demuren [58] employed second moment closure to model *Reynolds* stresses. He studied liquid jets in a crossflow for velocity ratios of 0.5 and 2, and obtained results in agreement with experimental data of Andreopoulos and Rodi [59], however, there remains many discrepancies. Similarly, Claus and Vanka [46] used $k-\varepsilon$ model and concluded that small eddies are damped out because the effective viscosity of fluid is increased and this results in misinterpretation of horseshoe vortex. They failed to obtain grid-independent results so the overprediction of turbulence levels could not be justified only based on shortcoming in modeling turbulence.

It should be mentioned that $k-\varepsilon$ model is capable of resolving some of the main features of the flow despite all of these contradictions and is the least computationally expensive among all turbulence models (except *Spalart-Allmaras* which is a one equation model), hence, used in this study.

1.3 Objectives

Depending on the illumination technique and analysis type different jet trajectories are predicted even for the same liquid type and operating conditions. On the other hand, most analytical studies calculate the penetration depth but do not suggest an explicit correlation for the jet trajectory which is the motivation of this work. The correlations that only utilize the liquid to gas momentum ratio are targeted at specific liquid and cannot be generalized for different liquids. Conversely, those correlations that do incorporate the liquid properties either directly or in terms of *Reynolds* number are derived for a certain range of freestream pressure and temperature, therefore they need to change their power index when the gas flow is heated or its pressure is elevated. Hence, the objectives of this study are as follows.

- Developing a theoretical correlation for elliptical jets in column breakup regime
- Formulating drag coefficients for elliptical profiles with various aspect ratios based on a 2-D model
- Simulating the deformation of circular liquid jets injected to gaseous crossflow using a 3-D model

1.4 Thesis outline

The theoretical approach is explained in chapter 2. All the details including the mathematical formulation and the final correlation are outlined.

In chapter 3, the numerical methodology is fully presented. This chapter covers *Volume of Fluid* model, turbulence model, discretization schemes, computational domain, boundary conditions, and the solver employed in this study.

Chapter 4 presents the results obtained from analytical and numerical approaches. The analytical results are validated against available experimental data in the literature for circular jets. In numerical part, 2-dimensional analysis is carried out to calculate the drag coefficients for elliptical profiles. The obtained drag coefficients are then used to predict the penetration depth of elliptical jets with various aspect ratios. Furthermore, a 3-dimensional model is used to simulate the liquid jet deformation subject to gaseous crossflows with various velocities.

Chapter 5 includes the conclusions of this work followed by useful suggestions for future studies.

2 Analytical approach

In this section, the jet in crossflow problem is simplified and the objective is to find an analytical correlation including the most important parameters. Figure 2-1 schematically shows an elliptical liquid jet in a uniform gaseous crossflow since the boundary layer thickness is expected to be less than 0.1 mm in the range of this study. U_∞ is the gas free stream velocity and V_j is the liquid jet velocity. x , y , and z axes represent freestream, vertical, and spanwise directions, respectively. The gas phase is assumed to be free of any shockwaves and its density and viscosity are determined by ideal gas law and Sutherland's law, respectively. The liquid has a constant density but its viscosity and surface tension vary with respect to the film temperature, i.e. average of freestream and liquid temperatures.

The jet is bent as the result of the drag force exerted by the crossflow, let θ represent the deflection angle, i.e. between crossflow direction (x axis) and normal direction to the jet centerline (n axis). δ is the thickness of an infinitesimal element, a and b are the axes of the ellipse in the freestream and spanwise directions, respectively. The aspect ratio of the elliptical jet is defined as b divided by a . The bottom floor is assumed to be solid wall except for the liquid exit which is mounted flush with this wall. The liquid exit is a simple orifice with an elliptical cross-section and the jet velocity profile is assumed to be uniform. The global coordinate (x - y) is fixed at the jet center on the bottom floor and the local coordinate (n - s) moves along the jet.

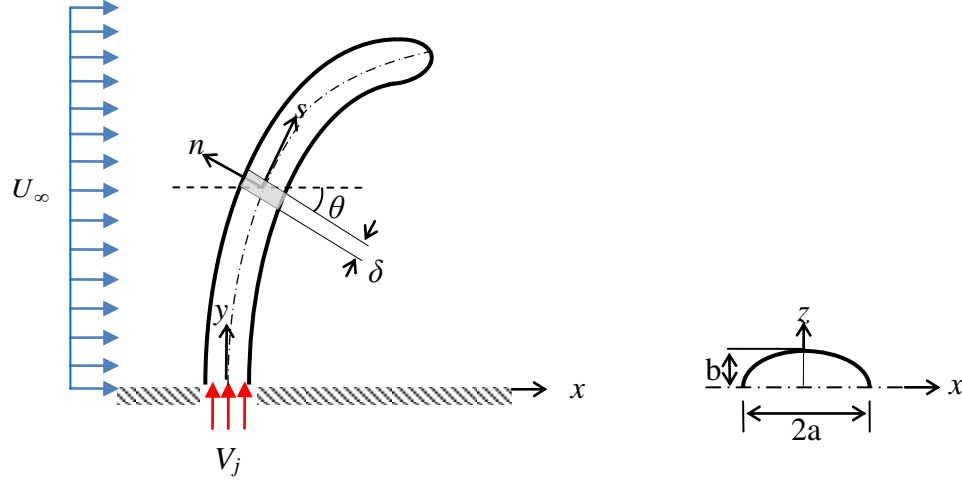


Figure 2-1: Schematic presentation of an elliptical liquid jet injected into a gaseous crossflow.

The balance of forces on the liquid element in the x -direction yields,

$$m \frac{du}{dt} = \sum F_x \quad (2-1)$$

where m is the mass of the element,

$$m = \rho_j \pi a b \delta \quad (2-2)$$

where the subscript j represents the jet properties. Since no evaporation and mass shedding occurs on the jet surface, the cross-sectional area of the jet is constant; hence, it is inferred from conservation of mass that V_j is invariant along the jet column (s -direction). Therefore, the projection of V_j on the x -axis yields,

$$u = V_j \sin \theta \quad (2-3)$$

The first time-derivative of u implies,

$$\frac{du}{dt} = V_j \cos \theta \frac{d\theta}{dt} \quad (2-4)$$

In column and multi-mode breakup regimes, i.e. $We < 60$ [23], the shear force is smaller than the aerodynamic force at relatively high velocities because the aerodynamic force is proportional to

U_∞^2 whereas the viscous force is proportional to U_∞ . Hence, the aerodynamic force is assumed to be the only force acting on the element,

$$\sum F_x = \frac{1}{2} C_D \rho_\infty u_n^2 (2b\delta) \cos \theta \quad (2-5)$$

where u_n is the normal component of the free stream velocity and C_D is the average drag coefficient acting on the jet column, hence it is constant. Substitution of equations (2-4) and (2-5) into (2-1) implies,

$$\rho_j \pi a b \delta (V_j \cos \theta) \frac{d\theta}{dt} = \frac{1}{2} C_D \rho_\infty (U_\infty \cos \theta)^2 (2b\delta) \cos \theta \quad (2-6)$$

which can be written as an ODE of the following form,

$$\frac{d\theta}{(\cos \theta)^2} = \left[\frac{C_D \rho_\infty}{\pi a \rho_j} \left(\frac{U_\infty^2}{V_j} \right) \right] dt \quad (2-7)$$

Let Ω represent the constant in the brackets, then $\tan \theta$ is found by integrating equation (2-7) with zero initial deflection,

$$\tan \theta = \Omega t \quad (2-8)$$

On the other hand,

$$\frac{dx}{dt} = V_j \sin \theta \quad (2-9)$$

Therefore,

$$\frac{dx}{dt} = V_j \frac{\Omega t}{\sqrt{1 + (\Omega t)^2}} \quad (2-10)$$

By integrating with zero initial condition, the variation of x with respect to time is found,

$$x = \frac{V_j}{\Omega} \left[\sqrt{1 + (\Omega t)^2} - 1 \right] \quad (2-11)$$

The jet vertical velocity is the projection of V_j on the y -axis,

$$\frac{dy}{dt} = V_j \cos \theta \quad (2-12)$$

θ is determined from equation (2-8) and substituted into equation (2-12), hence,

$$\frac{dy}{dt} = V_j \frac{1}{\sqrt{1 + (\Omega t)^2}} \quad (2-13)$$

First integration with zero initial condition implies,

$$y = \frac{V_j}{\Omega} \ln \left| \sqrt{1 + (\Omega t)^2} + \Omega t \right| \quad (2-14)$$

By eliminating the time from equations (2-11) and (2-14) the following equation is obtained,

$$y = \frac{V_j}{\Omega} \ln \left[\left(1 + \frac{\Omega}{V_j} x \right) + \sqrt{\left(1 + \frac{\Omega}{V_j} x \right)^2 - 1} \right] \quad (2-15)$$

Finally, a logarithmic correlation for the trajectory of jet centerline is achieved in dimensionless form,

$$\left(\frac{y}{a} \right) = \frac{\pi q}{C_D} \ln \left[1 + \frac{C_D}{\pi q} \left(\frac{x}{a} \right) + \sqrt{\left(1 + \frac{C_D}{\pi q} \left(\frac{x}{a} \right) \right)^2 - 1} \right] \quad (2-16)$$

where q is the liquid to gas momentum flux ratio and C_D represents the average drag coefficient on the liquid column. The choice of C_D depends on the jet aspect ratio, the gas *Reynolds* number, and liquid properties. Inamura [60] assumed C_D equal to 1 for circular jets whereas Wu *et al.* [26] proposed an average value of about 1.7 for water jets and equation (1-7) for other liquids. In a most recent work Mashayek *et al.* [32] developed series of equations (1-15) to (1-18) as a function of *Reynolds* number for various jet aspect ratios to calculate drag coefficient.

All the coefficients available in the literature are either rough estimates by averaging limited test cases or obtained from 2-D model of the jet cross-section. One of the drawbacks of calculating

the drag coefficient on a wall with no slip boundary condition is the rigidity. It is known that a liquid column is deformed because of the pressure distribution around its interface with gas which eventually changes its frontal area and hence the drag coefficient. In addition, the viscous force imposes an internal boundary layer within the liquid and no-slip boundary conditions will no longer hold. Therefore, full 3-D simulations of liquid jets in gaseous crossflow including all of the existing forces would be beneficiary which is the objective of the following chapter.

3 Numerical model

This section includes the methodology and formulation that has been employed in this study. The numerical model and available discretization schemes are briefly explained. At the end, the computational domain and applied boundary conditions are described in details.

Conservation of mass and momentum equations are solved for gas and liquid phases as well as an additional scalar equation for the advection of volume fraction.

Mass and momentum conservation equations for incompressible fluid can be stated as,

$$\nabla \cdot \vec{u} = 0 \quad (3-1)$$

$$\frac{\partial \vec{u}}{\partial t} + \nabla \cdot (\vec{u}\vec{u}) = -\frac{1}{\rho} \nabla p + \frac{1}{\rho} \nabla \cdot \vec{\tau} + \vec{g} + \frac{1}{\rho} \vec{F}_b \quad (3-2)$$

where \vec{u} represents the velocity vector, p the pressure, ρ the fluid density, \vec{g} the gravitational acceleration, and \vec{F}_b is the total body force (per unit volume) acting on the fluid. $\vec{\tau}$ is the shear stress tensor and for a Newtonian fluid it can be written as,

$$\vec{\tau} = \mu (\nabla \vec{u} + (\nabla \vec{u})^T) \quad (3-3)$$

where μ is the dynamic viscosity of the fluid.

Surface tension force is defined as the pressure jump at the interface. This force is applied by implementing the *Continuum Surface Force (CSF)* model proposed by Brackbill *et al.* [61]. In the *CSF* model surface tension force is calculated as follows.

$$\vec{F}_{ST}(\vec{x}) = \sigma \int_S \kappa(\vec{y}) \hat{n}(\vec{y}) \delta(\vec{x} - \vec{y}) dS \quad (3-4)$$

where σ is the liquid surface tension at the interface, κ is the local curvature, \hat{n} is the local unit normal to the interface, and δ is the Dirac delta function. In equation (3-4), S corresponds to the area of the free surface. \vec{x} and \vec{y} are vectors indicating the location in which the force is

calculated and the location of free surface, respectively. Curvature, κ , is defined as divergence of the unit normal vector,

$$\kappa = -\nabla \cdot \hat{n} \quad (3-5)$$

The unit normal vector is calculated from equation (3-6),

$$\hat{n} = \frac{n}{|n|} \quad (3-6)$$

where n is surface normal and is defined as the gradient of volume fraction.

$$n = \nabla f \quad (3-7)$$

Surface tension force can be expressed as a source term using the divergence theorem and can be added to the momentum equation as expressed in equation (3-8).

$$F_{ST} = \sigma \frac{\rho \kappa \nabla f}{\frac{1}{2}(\rho_l + \rho_g)} \quad (3-8)$$

where ρ is the volume-averaged density computed from equation (3-9).

$$\rho = f\rho_l + (1-f)\rho_g \quad (3-9)$$

3.1 Volume of Fluid (VOF) method

To model multi-phase flows there are currently two general approaches available; Eulerian and Lagrangian methods. In Eulerian methods, the grid is fixed, hence does not move with the interface. Conversely, in Lagrangian methods the grid is moving with the interface velocity. In both approaches the grid may be structured or unstructured. Since the interface between the two phases with different densities is a discontinuity in the computational cells, special resolution is required at the free surface to capture this discontinuity. Eulerian method has shown to be more

rigorous in resolving the interface between two phases. There are various Eulerian methods available, e.g. Height Functions, Line Segments, and Marker method. One of the widely used Eulerian methods which has been shown to be very promising is *Volume of Fluid (VOF)* model. In *VOF*, a scalar field is defined for volume fraction of liquid phase and its value depends on the fraction of the cell volume occupied by this phase.

$$\begin{cases} f = 0 & \text{Gas phase} \\ 0 < f < 1 & \text{Interface} \\ f = 1 & \text{Liquid phase} \end{cases} \quad (3-10)$$

The values between zero and one represent the interface of two phases, schematically shown in figure 3-1.

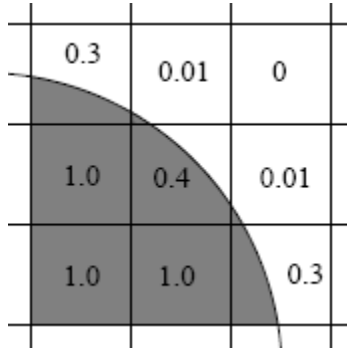


Figure 3-1: Volume fraction representation in each cell containing both phases.

Since the volume fraction represents the volume occupied by the liquid, it should be advected by the flow field. The following equation governs the advection of volume fraction f .

$$\frac{\partial f}{\partial t} + \nabla \cdot (\vec{V}f) = 0 \quad (3-11)$$

Following the advection, the interface is reconstructed using the *Piecewise Linear Interface Calculation (PLIC)* proposed by Youngs [62]. In *PLIC* method, the interface is defined at each computational cell by a slope and an intercept. The slope of the interface is calculated based on the volume fractions of neighboring cells as presented in figure 3-2.

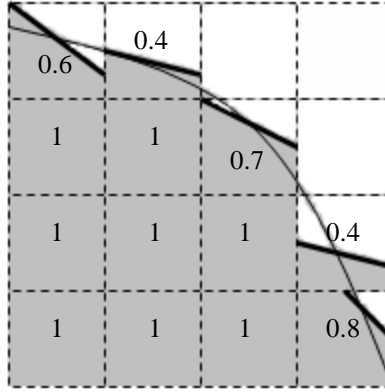


Figure 3-2: Piecewise Linear Interface Calculation (PLIC) representation of an interface.

The algorithm can be summarized in three main steps,

1. Determining the normal direction to the linear interface in a partially-filled cell by solving equation (3-7); this helps to construct the linear interface.
2. Determining the velocity and direction of the moving interface, to find the displacement of interface through each computational cell at one time step. In this step the advection equation (3-11) has to be solved.
3. Determining the volume fraction in each cell using the balance of fluxes calculated during step 2.

It should be mentioned that the accuracy of interface reconstruction depends on mesh resolution which renders *VOF* methods grid dependent.

The time step during for all the advective fluxes in transport equations is different from one used in *VOF* calculation. Time step in *VOF* is adaptive and depends on the *CFL* condition defined as,

$$CFL = \frac{\Delta t \cdot u_{fluid}}{\Delta x} \quad (3-12)$$

Thus, the time step is restricted by maximum *CFL* given as input and the time required for the fluid to empty out one cell has to satisfy the following inequality,

$$\max \left[\frac{|u|\Delta t}{\Delta x}, \frac{|v|\Delta t}{\Delta y}, \frac{|w|\Delta t}{\Delta z} \right] < 1 \quad (3-13)$$

and fluid is not allowed to be diffused more than one cell at each time step, which requires the following condition.

$$\Delta t < \frac{\rho}{\mu} \cdot \min \left[\frac{(\Delta x)^2(\Delta y)^2}{(\Delta x)^2 + (\Delta y)^2}, \frac{(\Delta x)^2(\Delta z)^2}{(\Delta x)^2 + (\Delta z)^2}, \frac{(\Delta z)^2(\Delta y)^2}{(\Delta z)^2 + (\Delta y)^2} \right] \quad (3-14)$$

Brackbill *et al.* [61] proposed another time limitation in modeling surface tension force as,

$$\Delta t < \sqrt{\frac{\rho}{4\pi\sigma}} \min \left[(\Delta x)^{3/2}, (\Delta y)^{3/2}, (\Delta z)^{3/2} \right] \quad (3-15)$$

which the latter is usually less restrictive than the first two limitations.

3.2 Turbulence model

In *Reynolds* averaging, the solution variables in the exact Navier-Stokes equations are decomposed into a time or ensemble averaged term, and a fluctuating term, e. g. the velocity component can be expressed as,

$$\vec{u} = \bar{\vec{u}} + \vec{u}' \quad (3-16)$$

where $\bar{\vec{u}}$ and \vec{u}' are the mean and fluctuating components, respectively.

Substituting variables of this form into the instantaneous continuity and momentum equations yields,

$$\frac{\partial}{\partial t}(\rho) + \nabla \cdot (\rho \vec{u}) = 0 \quad (3-17)$$

and,

$$\frac{\partial}{\partial t}(\rho \bar{u}) + \nabla \cdot (\rho \bar{u} \bar{u}) = -\nabla p + \nabla \cdot \bar{\tau} + \nabla \cdot (-\rho \overline{u'u'}) \quad (3-18)$$

where the stress tensor is expressed as,

$$\bar{\tau} = \mu \left[(\nabla \bar{u} + \nabla \bar{u}^T) - \frac{2}{3} \nabla \cdot \bar{u} I \right] \quad (3-19)$$

In equation (3-19), I is the identity matrix. Equations (3-17) and (3-18) are called the *Reynolds Averaged Navier-Stokes (RANS)* equations. The *Reynolds* stress term, $-\rho \overline{u'u'}$, should be appropriately modeled to close the system of equations. Hence, the first moment of closure is used to relate the *Reynolds* stresses to the mean velocity gradients based on Boussinesq's hypothesis,

$$-\rho \overline{u'_i u'_j} = \mu_t \left(\frac{\partial u_i}{\partial x_j} + \frac{\partial u_j}{\partial x_i} \right) - \frac{2}{3} \left(\rho k + \frac{\partial u_k}{\partial x_k} \right) \delta_{ij} \quad (3-20)$$

where k is turbulence kinetic, μ_t is turbulent viscosity, and δ is Dirac delta function.

The advantage of this approach is the relatively low computational cost associated with the computation of the turbulent viscosity. Two additional transport equations for the turbulence kinetic energy, k , and turbulence dissipation rate, ε are solved; then, μ_t is computed as a function of k and ε . The disadvantage of Boussinesq's hypothesis is that it assumes μ_t is an isotropic scalar quantity, which is not strictly true for all conditions.

The standard $k - \varepsilon$ model proposed by Launder and Spalding [63] is known to be slightly over-diffusive in certain situations, while the *RNG* $k - \varepsilon$ model is designed such that the turbulent viscosity is reduced in response to high rates of strain. These characteristics make it more responsive to important physical instabilities such as time-dependent turbulent vortex shedding.

The *RNG* $k - \varepsilon$ model is based on the assumption that the flow is fully turbulent and the effect of molecular viscosity is negligible. It is derived from instantaneous Navier-Stokes equations using

a mathematical technique called *Re-Normalization Group (RNG)* theory. The reader is referred to [64] and [65] for the details.

In *RNG* $k-\varepsilon$ Model, turbulent kinetic energy, k , and its dissipation, ε , are obtained by solving two transport equations as,

$$\frac{\partial}{\partial t}(k) + \frac{\partial}{\partial x_i}(k u_i) = \frac{\partial}{\partial x_j} \left(\alpha_k \nu_t \frac{\partial k}{\partial x_j} \right) + \nu_t S^2 - \varepsilon \quad (3-21)$$

$$\frac{\partial}{\partial t}(\varepsilon) + \frac{\partial}{\partial x_i}(\varepsilon u_i) = \frac{\partial}{\partial x_j} \left(\alpha_\varepsilon \nu_t \frac{\partial \varepsilon}{\partial x_j} \right) + C_{1\varepsilon} \frac{\varepsilon}{k} \nu_t S^2 - C_{2\varepsilon}^* \frac{\varepsilon^2}{k} \quad (3-22)$$

where the quantities α_k and α_ε are the inverse effective Prandtl numbers for k and ε , respectively.

These parameters are obtained from the analytical solution by *RNG* theory [64], [65].

ν_t is the turbulent viscosity calculated as follows.

$$\nu_t = C_\mu \frac{k^2}{\varepsilon}, \quad C_\mu = 0.0845 \quad (3-23)$$

S is the modulus of the mean rate-of-strain tensor, defined as,

$$S \equiv \sqrt{2S_{ij}S_{ij}} \quad (3-24)$$

where S_{ij} is calculated from Boussinesq's hypothesis.

$$S_{ij} = \frac{1}{2} \left(\frac{\partial u_i}{\partial x_j} + \frac{\partial u_j}{\partial x_i} \right) \quad (3-25)$$

The coefficient in equation (3-22) is defined as,

$$C_{2\varepsilon}^* \equiv C_{2\varepsilon} + \frac{C_\mu \eta^3 (1 - \eta / \eta_0)}{1 + \beta \eta^3} \quad (3-26)$$

where,

$$\eta = Sk / \varepsilon \quad (3-27)$$

and the constants in (3-26) are as follows.

$$\eta_0 = 4.38, \beta = 0.012, C_{1\epsilon} = 1.42, C_{2\epsilon} = 1.68 \quad (3-28)$$

It is computationally very expensive and rather unnecessary to resolve the laminar sublayer because the grid size has to be very small near the wall. Thus, a standard wall function proposed by Launder and Spalding [50] is used to specify the boundary condition for mean velocity adjacent to wall. This wall function is based on a logarithmic law to link the wall to the fully-turbulent region and omit viscous sub-layer in between. Therefore, the characteristic velocity is related to the dimensionless distance to the wall as follows.

$$U^* = \frac{1}{\kappa} \ln(Ey^*) \quad (3-29)$$

where κ is von Karman constant equal to 0.4187 and E is an empirical constant equal to 9.793. The velocity and wall distance are defined based on turbulent properties by the following relations,

$$U^* \equiv \frac{U_P C_\mu^{1/4} k_P^{1/2}}{\tau_w / \rho} \quad (3-30)$$

and,

$$y^* \equiv \frac{\rho C_\mu^{1/4} k_P^{1/2} y_P}{\mu} \quad (3-31)$$

where U_P , k_P and y_P are the mean velocity of the fluid, the turbulence kinetic energy at point P and distance from point P to the wall, respectively.

Logarithmic law is applied for values of y^* greater than 11.225 and for the values less than 11.225 the laminar stress-strain is assumed as,

$$U^* \equiv y^* \quad (3-32)$$

While using this wall function one should make sure that the mesh is fine enough close to the

wall, and the centroid of the cell adjacent to the wall should not fall into the viscous sub-layer or the buffer layer regions.

The source terms in k -equation are obtained based on equilibrium hypothesis. This requires that in the wall-adjacent control volume the production of k is equal to its dissipation rate, thus,

$$G_k \approx \tau_w \frac{\partial U}{\partial y} \quad (3-33)$$

Using equations (3-29) and (3-30) results in,

$$G_k = \tau_w \frac{\tau_w}{\kappa \rho C_\mu^{1/4} k_P^{1/2} y_P} \quad (3-34)$$

Furthermore, a similar expression for the dissipation rate can be obtained.

$$\varepsilon_P = \frac{C_\mu^{3/4} k_P^{3/2}}{\kappa y_P} \quad (3-35)$$

3.3 Solver and discretization schemes

Pressure-Based Segregated Algorithm is chosen as the solver. Mass and momentum equations were solved with first-order implicit scheme for temporal terms and second-order upwind method for space. Since the grid arrangement is staggered, some quantities such as pressure need to be calculated at the center of cell faces by interpolation from adjacent cell centers. Therefore, *PREssure STaggering Option (PRESTO!)* scheme is used which offers comparable accuracy for non-structured grids. For pressure-velocity coupling in the momentum equation, *Pressure-Implicit with Splitting of Operators (PISO)* algorithm with one neighbor and skewness correction was employed to reduce the internal iteration per time step required for convergence. *Modified High Resolution Interface Capturing (HRIC)* has been used to discretize advection equation. *FLUENT 6.3* was used as the solver.

3.4 Boundary conditions

In general there are four types of boundary conditions encountered in this study; velocity inlet, pressure outlet, wall, and symmetry boundary condition. Depending on the type of analysis boundary conditions are defined in two sections; 2-D and 3-D models.

3.4.1 2-D model

A 2-D analysis is carried out to calculate the drag coefficient for elliptical profiles with aspect ratios less than 1 which to the best of our knowledge is not available in open literature. Being computationally less expensive it allows extensive grid dependency study, up to third order accurate discretization scheme for convective terms and turbulent scalars, different domain sizes based on freestream *Reynolds* number. The domain size and boundaries are schematically shown in figure 3-3.

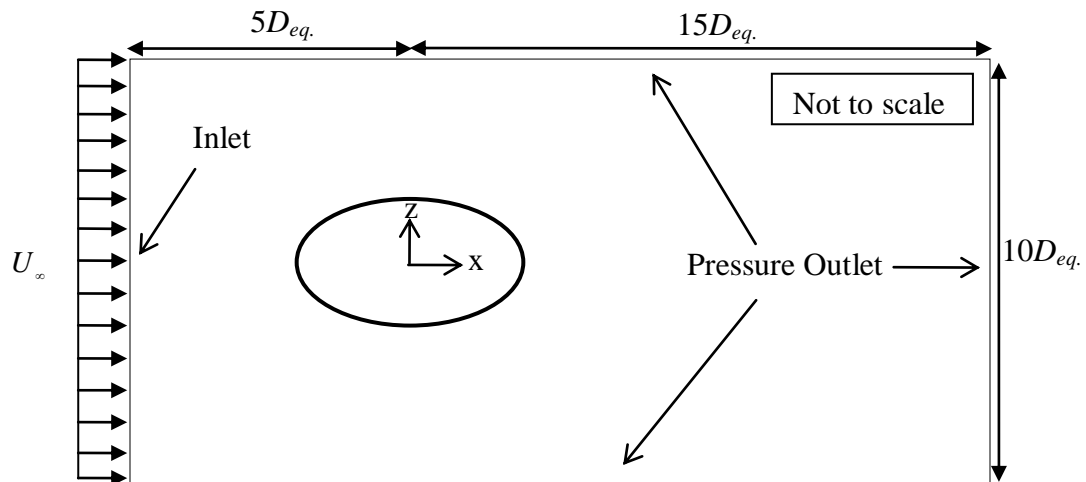


Figure 3-3: Computational domain and boundary types for 2-D model.

Velocity inlet: a uniform freestream is assumed at the inlet with zero spanwise velocity.

$$u(\text{inlet}) = U_{\infty} \quad (3-36)$$

Pressure outlet: far from the elliptical shape, the pressure is assumed to be constant and set to ambient value.

Wall: on the ellipse surface no-slip and no-penetration boundary conditions are imposed as follows.

$$u = v = 0 \quad (3-37)$$

$$\frac{\partial u}{\partial n} = \frac{\partial v}{\partial n} = 0 \quad (3-38)$$

3.4.2 3-D model

Since the cross section of the liquid jet is deformed as exposed to gas transverse flow, a 3-D model is able to resolve more features of liquid jets injected into a crossflow. Figure 3-4 illustrates the domain size and all the boundaries imposed on various faces. H , W and L are the height, width, and length of the computational domain and equal to 30, 7, and 10 jet radii, respectively. The crossflow has a uniform profile and is aligned in the x -direction. The liquid jet is discharged in the y -direction and the coordinate origin is located at the center of the jet exit. The z -axis shows the spanwise direction and the x - z plane is a solid wall except at the jet exit which is mounted flush on this plane. Since the flow is assumed to be symmetric about the center plane of liquid jet, i.e. x - y plane, only half of domain is modeled. The boundary conditions for the 3-D model are as follows.

Gas crossflow inlet: since the boundary layer thickness is estimated to be less than 0.1 mm for the flow conditions of this study we neglect boundary layer effect because of flat wall and assume a uniform gas flow.

$$\begin{cases} u(x=0, y, z) = U_\infty \\ v(x=0, y, z) = 0 \\ w(x=0, y, z) = 0 \end{cases} \quad (3-39)$$

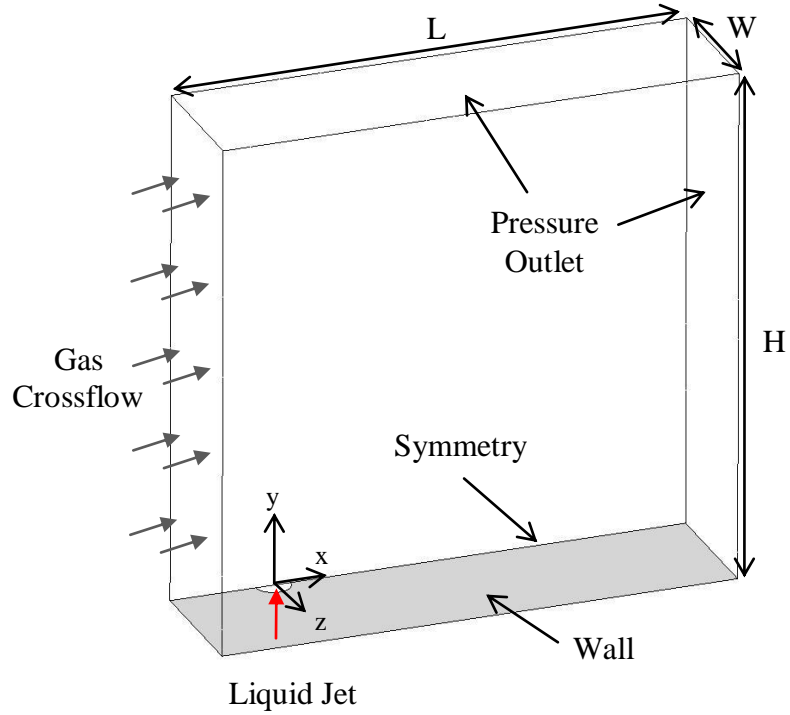


Figure 3-4: Computational domain and boundary types for 3-D model.

Liquid jet inlet: a fully developed pipe flow is assumed at the liquid inlet boundary hence nozzle is not modeled and a parabolic velocity profile is defined in the y-direction and other velocity components are set to zero.

$$\begin{cases} u(x, y=0, z) = 0 \\ v(x, y=0, z) = 2V_j \left(1 - \left(\frac{x}{b} \right)^2 - \left(\frac{z}{a} \right)^2 \right) \\ w(x, y=0, z) = 0 \end{cases} \quad (3-40)$$

where, V_j is the jet mean velocity.

Symmetry: to reduce the computational effort, only half of the domain is modeled and a symmetry boundary condition is imposed at the center plane of the nozzle. It requires that the velocity component normal to this plane and z -gradient of other variable are set to zero, hence,

$$\begin{cases} w(x, y, z = 0) = 0 \\ \frac{\partial}{\partial z} = 0 \end{cases} \quad (3-41)$$

Pressure outlet: far from the jet, the pressure is assumed to be constant and set to ambient value.

Wall: discharging orifice is mounted flush with the ground floor. Hence, this plane is set to wall boundary except for the jet exit. Therefore, no-slip and no-penetration boundary conditions are imposed on the wall.

$$u = v = w = 0 \quad (3-42)$$

$$\frac{\partial}{\partial n} = 0 \quad (3-43)$$

where n indicates the normal direction and is replaced by x , y , and z depending on the boundary planes.

Finally, the values of k and ε at node P adjacent to wall is found from the logarithmic law explained in §3.2.

$$k_P = \frac{u_\tau^2}{\sqrt{C_\mu}} \quad (3-44)$$

$$\varepsilon_P = \frac{u_\tau^3}{\kappa y_P} \quad (3-45)$$

where u_τ is friction velocity defined as follows.

$$u_\tau = \frac{\tau_w}{\rho} \quad (3-46)$$

4 Results and discussions

4.1 2-D numerical results

As previously discussed in §1.2.2 the drag coefficients are available for circular profiles and elliptical profiles with aspect ratios greater than one. Hence, we only focus on the aspect ratio of one for validation of the present model and aspect ratios less than one. In this regard, elliptical profiles with aspect ratios of 1, 0.5, and 0.25 are chosen for simulations. The freestream velocity is varied to obtain *Reynolds* numbers of 150, 600, 1000, 2000, 4000, and 8000. To calculate the total drag coefficient of each profile the following procedure is carried out for all the *Reynolds* numbers.

In general, the drag force exerted on jet cross-section is composed of two components; pressure and friction drags expressed as equation (4-1).

$$D = D_p + D_f \quad (4-1)$$

where D is the drag force and the subscripts p and f represent pressure and friction components, respectively. Figure 4-1 illustrates the forces exerted by pressure and shear stress on infinitesimal area, dA ,

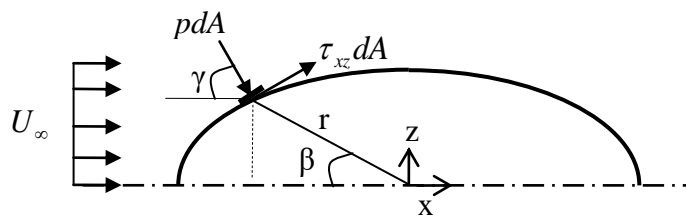


Figure 4-1: Drag coefficient over half of an elliptical cylinder.

The angle between normal to the interface and the x -axis, γ , is found from gradient of the interface as explained below.

Let $s(x,z)$ represent the surface of the ellipse in the x - z plane,

$$s(x, z) = \left(\frac{x}{a}\right)^2 + \left(\frac{z}{b}\right)^2 - 1 \quad (4-2)$$

Then normal to the surface is found from the gradient of s .

$$\vec{n} = \nabla s = 2\frac{x}{a^2}\hat{e}_x + 2\frac{z}{b^2}\hat{e}_z \quad (4-3)$$

Hence,

$$\tan(\gamma) = -\frac{z}{x}\left(\frac{a}{b}\right)^2 \quad (4-4)$$

Pressure drag is defined as the projection of pressure force on the x -axis,

$$D_p = \int_0^\pi p \cos \gamma \, dA \quad (4-5)$$

where dA is the area of unit depth segment. Similar expression for friction drag yields,

$$D_f = \int_0^\pi \tau_{xz} \sin \gamma \, dA \quad (4-6)$$

The drag coefficients are consequently obtained by dividing the drag force by free stream dynamic pressure times the projected area, A ,

$$C_D = \frac{D}{\frac{1}{2}\rho_g U_\infty^2 A} \quad (4-7)$$

where D is the total drag force, hence, the pressure drag coefficient yields,

$$C_{D_p} = \frac{2}{\rho_g U_\infty^2 A} \int_0^\pi p \cos \gamma \, dA \quad (4-8)$$

Similarly for friction drag,

$$C_{D_f} = \frac{2}{\rho_g U_\infty^2 A} \int_0^\pi \tau_{xz} \sin \gamma dA \quad (4-9)$$

In order to evaluate the accuracy of the 2-D model, the total drag coefficients for a circular profile are calculated at six *Reynolds* numbers from 150 up to 8000. The results obtained from the present model are compared against equation (1-15) proposed by Mashayek *et al.* [32] and presented in figure 4-2.

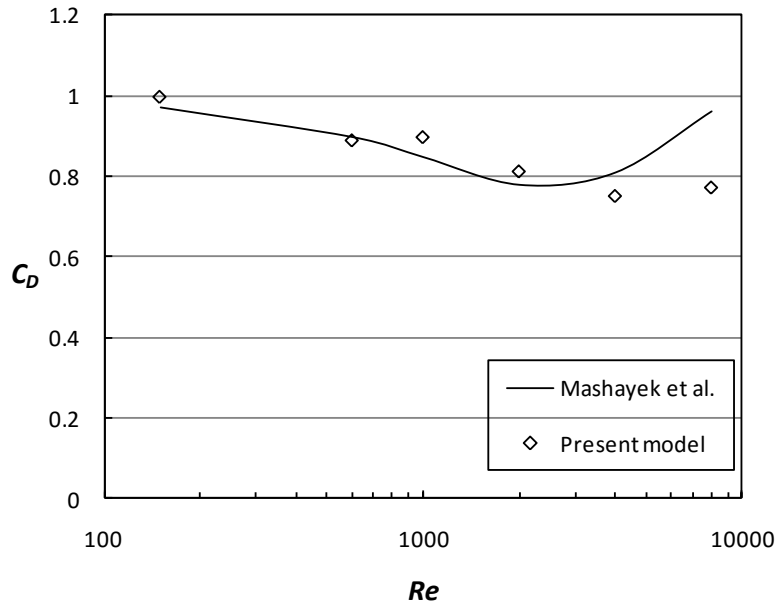


Figure 4-2: Drag coefficient plotted versus *Reynolds* number for a circular profile.

The symbols in the figure indicate the *Reynolds* numbers chosen for calculations and the average error is 2.6 percent compared to the correlation of Mashayek *et al.* [32]. The drag coefficients calculated from the 2-D model are within acceptable accuracy for the abovementioned range of

Reynolds number. Therefore the same model is employed to obtain the drag coefficients for elliptical profiles with aspect ratios of 0.25 and 0.5; the results are presented in figure 4-3.

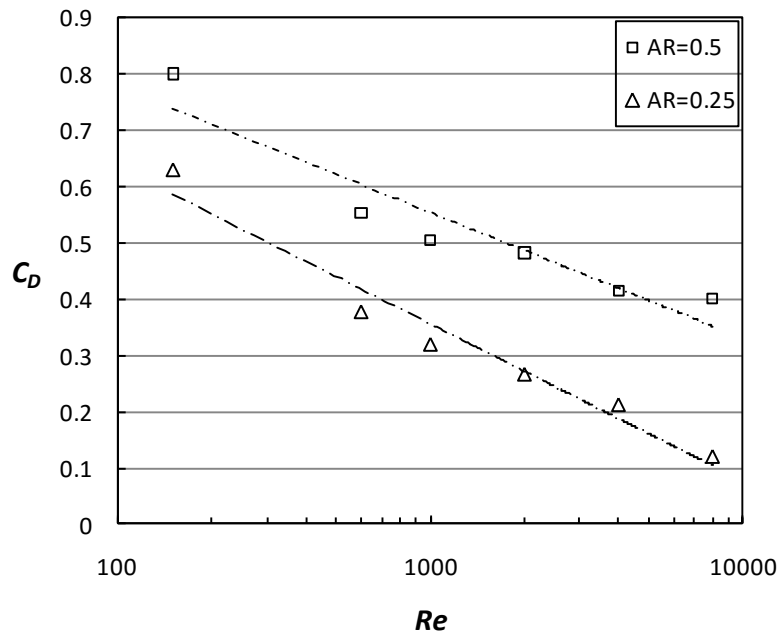


Figure 4-3: Drag coefficient plotted versus *Reynolds* number for aspect ratios of 0.5 and 0.25.

It should be mentioned that the symbols show the *Reynolds* numbers chosen for simulations and the lines represent the fitted curves for each aspect ratio. Thus, two logarithmic correlations are found for aspect ratios of 0.5 and 0.25 as follows.

$$\text{AR}=0.5: C_D = -0.097 \ln(\text{Re}) + 1.2263 \quad (4-10)$$

$$\text{AR}=0.25: C_D = -0.121 \ln(\text{Re}) + 1.1928 \quad (4-11)$$

In the following section, to predict the jet trajectory of elliptical jets with aspect ratios of 0.5 and 0.25 equations (4-10) and (4-11) are used, respectively.

4.2 Analytical solutions

In this section the analytical correlation developed in §2 is used to calculate the jet trajectories for momentum ratios up to 100. First, the accuracy of the proposed analytical model is validated against experimental data available in the literature for circular jets. Then, the centerline trajectories of elliptical jets with various aspect ratios are presented using the 2-D results obtained in §4.1.

Figure 4-4 illustrates the jet trajectories predicted by the present model and the comparisons with various experimental correlations. It should be noted that a drag coefficient of 1.7 was used for all the cases in the present model; furthermore, the present correlation integrates the effect of gas velocity and its properties in terms of the drag coefficient.

It can be seen in figure 4-4 that the present model agrees well with the measurement of Wu *et al.* [26] with an average error of less than 2.28 percent. It should be mentioned that the present correlation is derived based on the assumption that the only acting force on liquid column is the aerodynamic force and other forces, i.e. viscous and surface tension forces are negligible. Furthermore, the rate of mass stripping from the jet surface and the liquid evaporation are ignored.

Since there is no universally accepted choice for C_D in the literature, first C_D is considered to be equal to 1.7 as proposed by Wu *et al.* [26]. In another case, C_D of unity is assumed according to Inamura [60], and finally in the third case, C_D is calculated based on equation (1-15). Figure 4-5 illustrates the effect of drag coefficient on the jet penetration depth. For all the drag coefficients the jet trajectory is closely followed by the present work for momentum ratios of 100, 50, and 10 with an average error of less than 2.28 percent. This implies that current model is capable of predicting the penetration depth by adjusting the drag coefficients properly.

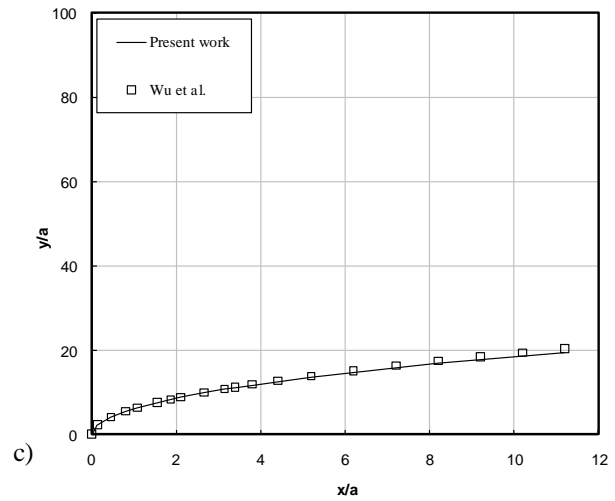
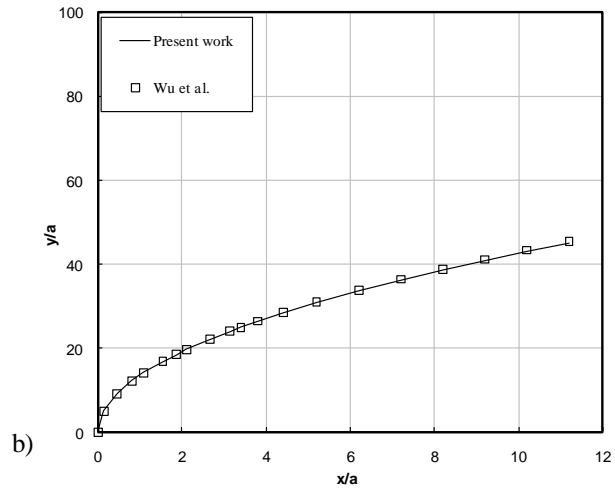
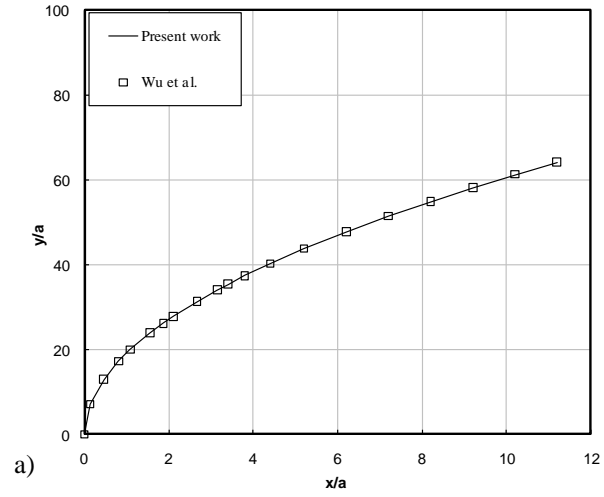


Figure 4-4: Trajectory of water jet injected into air crossflow for momentum ratios equal to (a) 100, (b) 50, and (c) 10.

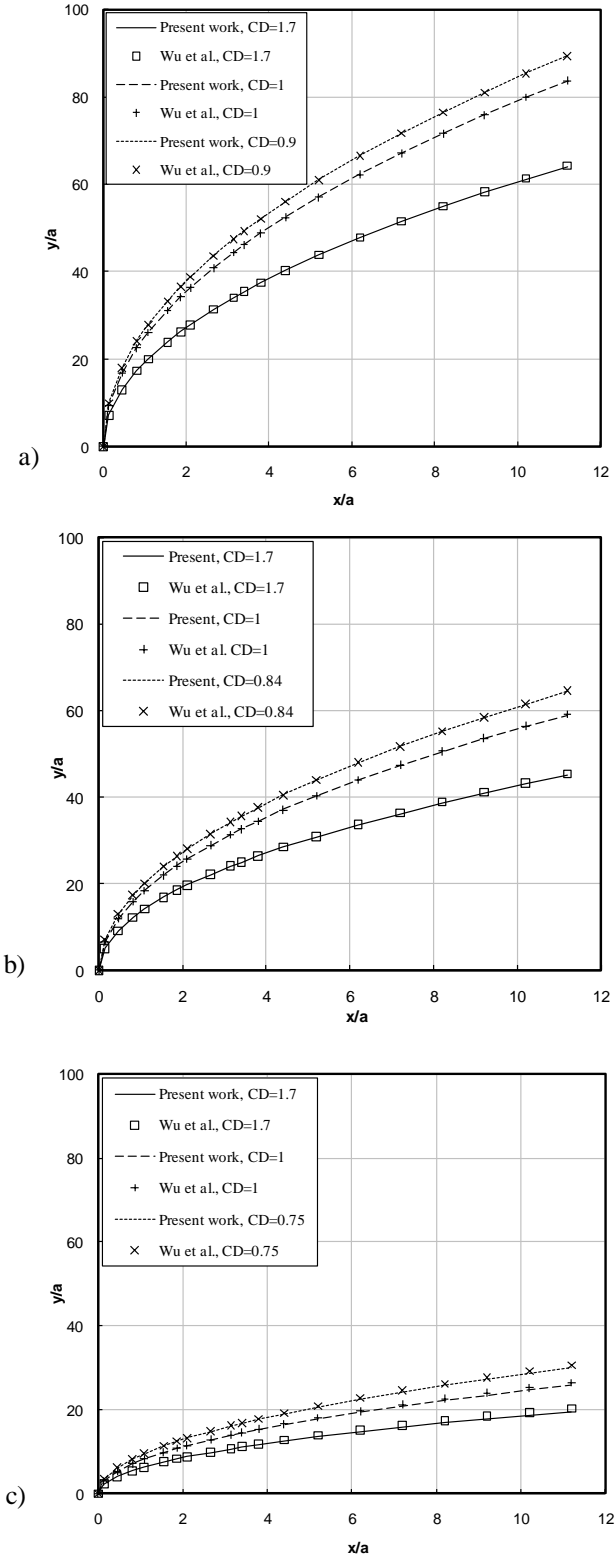


Figure 4-5: Effect of drag coefficient on the water jet trajectory; momentum ratios of (a) 100, (b) 50, and (c) 10 compared to experiments of Wu *et al.* [26].

The correlation presented in this work is valid for near-field trajectory of the jet in column breakup regime where liquid core is observed. As the freestream *Weber* number increases, small liquid droplets will start to strip off from the surface of the jet and the assumption of constant element mass will not hold. To illustrate the effect of freestream *Weber* number on the jet penetration, two *Weber* numbers of 27.8 and 52.5 are chosen with a constant momentum ratio of 18 and compared with experimental data of Stenzler *et al.* [29] presented in figure 4-6.

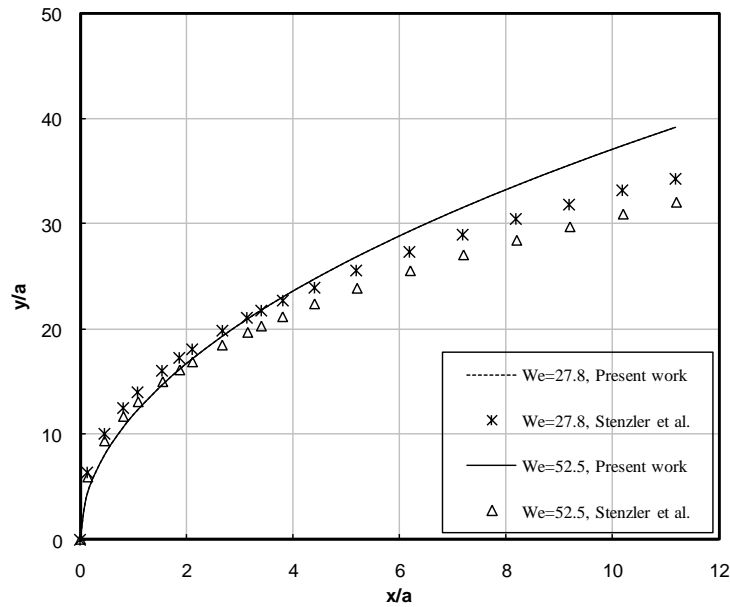


Figure 4-6: Trajectory of water jet injected into air crossflow for two different *Weber* numbers and a constant momentum ratio of 18.

It should be mentioned that the correlation of Stenzler *et al.* [29] uses directly the freestream *Weber* number with a power index of -0.11. On the other hand, the present model incorporates the gas velocity in the drag coefficient of the jet. For *Weber* number equal to 27.8 the centerline trajectory predicted by the present correlation deviates from the results of Stenzler *et al.* [29] by

2.66 percent in average error and in the case of 52.5 *Weber* number this error is increased to 7.60 percent. Hence, at high *Weber* numbers the accuracy of the present correlation is reduced.

To study the effect of liquid properties, the trajectories of different liquid jets are calculated based on present correlation and compared against experimental data of Wu *et al.* [26]. Figure 4-7 illustrates the effect of liquid properties on the jet penetration for a momentum ratio equal to 50. The predicted trajectories for water, ethyl alcohol and glycerol mixtures agree well with data of Wu *et al.* [26] with an average error of less than 1 percent.

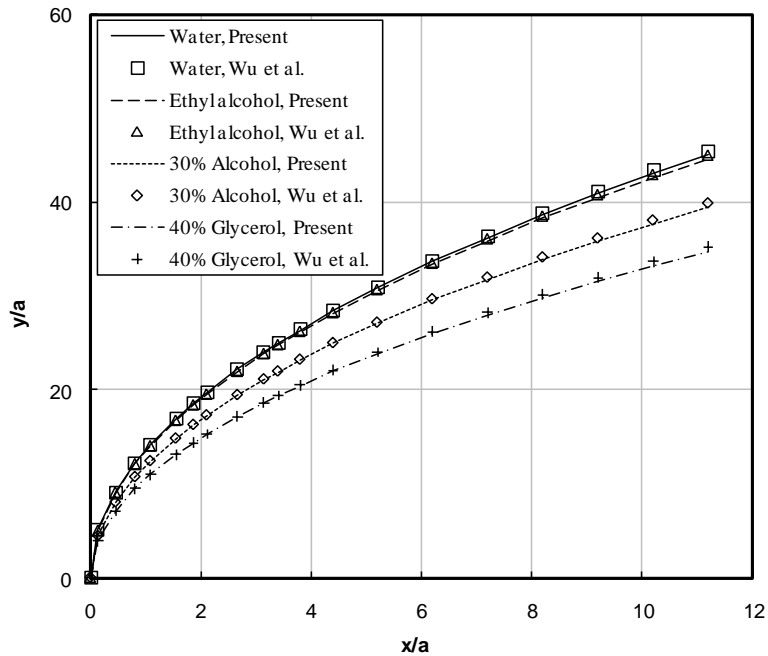


Figure 4-7: Jet trajectory for different liquids; momentum ratio of 50.

Ethyl alcohol has lower density than water (781 compared to 998 kg/m³) which somehow neutralizes its higher viscosity. In general, liquids with higher density and lower viscosity tend to penetrate more. Alcohol and glycerol mixtures have higher viscosities than water therefore, they are expected to have lower penetration depth which is shown by experiments and predicted by

the present correlation since the drag coefficient increases with viscosity based on equation (2-16). On the other hand 30% alcohol has a density slightly lower than water (958 kg/m^3) but its viscosity is more than twice of water viscosity, hence, it penetrates less. The glycerol/water mixture has the highest density (1113 kg/m^3) and its viscosity is more than four times of that of water which dramatically reduces its penetration. To further study the effect of liquid properties the experiments of Stenzler *et al.* [29] have been used for comparison at momentum ratio of 18 and the results are presented in figure 4-8.

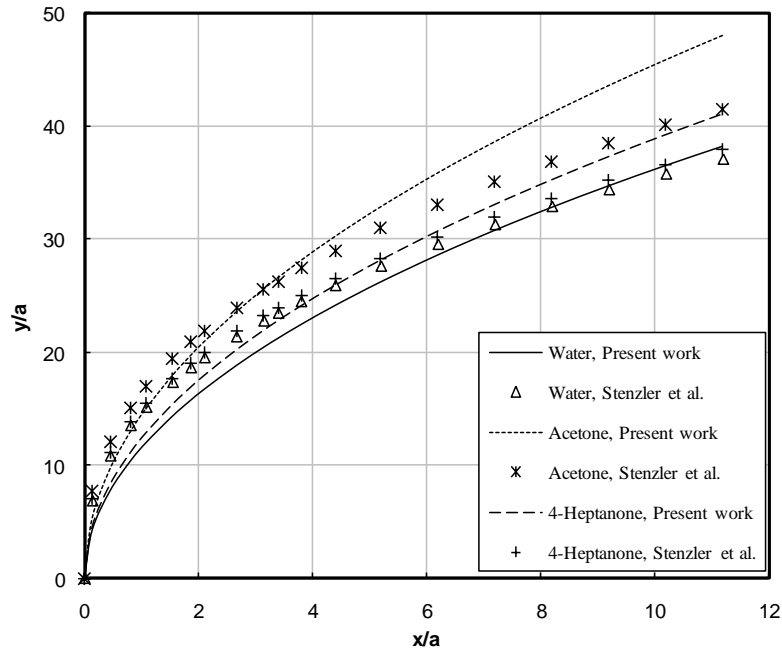


Figure 4-8: Jet trajectory for different liquids; momentum ratio of 18.

It is inferred from the results that the correlation proposed in this work is able to predict the trend observed in the experimental results although it underpredicts the data of Stenzler *et al.* [29] for water with an average error of 7 percent. Moreover, the penetrations of 4-Heptanone and Acetone are overpredicted by 2.5 percent and 4 percent, respectively. This deviation could be

due to the lack of modifications for surface tension and viscous forces in the theoretical model. The *Weber* number for Acetone and 4-Heptanone is 15.7 and in the case of water is equal to 13.9. Since the surface tension for Acetone and 4-Heptanone is the same (0.0235 N/m), their trajectories are comparable. The density of 4-Heptanone is higher than Acetone (816 compared to 790 kg/m³) but the fact that Acetone has lower viscosity allows it to penetrate more. To take into account the effect of the viscosity, C_D for water is calculated by equation (1-15) and is used to find the drag coefficients for Acetone and 4-Heptanone from equation (1-7). 4-Heptanone has higher C_D which explains why it penetrates slightly less than Acetone as predicted by present work. In the case of water the *Weber* number is lower, thus higher penetration is expected. The density and viscosity of water are the highest among three cases, as well as its surface tension (0.0728 N/m) which is more than three times of that of Acetone and 4-Heptanone. This results in an increase of crossflow velocity at constant momentum ratio which consequently causes the drag exerted on the jet to increase, hence, the penetration depth is reduced.

In order to examine the accuracy of the present model at elevated temperatures and pressures, the experimental data of Ragucci *et al.* [30] have been used. Figure 4-9 illustrates the effect of pressure and temperature on the water jet trajectories for a momentum ratio of 50. The deviation of the trajectories predicted by present correlation compared to experiments at elevated temperature and pressure is speculated to be the result of neglecting the evaporation and mass stripping from the jet surface. Although current work overpredicts the trajectories, it shows an acceptable trend. When the free stream temperature increases while its pressure is kept constant, the gas density is reduced. Therefore, the gas velocity has to increase for a constant momentum ratio provided that the liquid velocity is the same and its density is not much affected by an increase in the temperature. On the other hand, the gas viscosity is proportional to $T^{3/2}$ from

Sutherland's law and gas density is proportional to reciprocal of temperature for constant pressure. Since the term $\rho_g U_\infty^2$ is kept constant then the *Reynolds* number would be proportional to T^{-1} . As a result of increasing the air temperature at constant pressure, *Reynolds* number and drag coefficient are reduced, thus, the jet penetrates more into the crossflow although the variations are not significant.

On the other hand, when the pressure is increased while the temperature is kept constant the gas viscosity does not change but the density increases proportional to p . Because surface tension and $\rho_\infty U_\infty^2$ are kept constant, the *Weber* number does not change but U_∞ decreases proportional to $p^{-1/2}$. Overall it results in a decrease in *Reynolds* number and drag coefficient, hence, the penetration is enhanced.

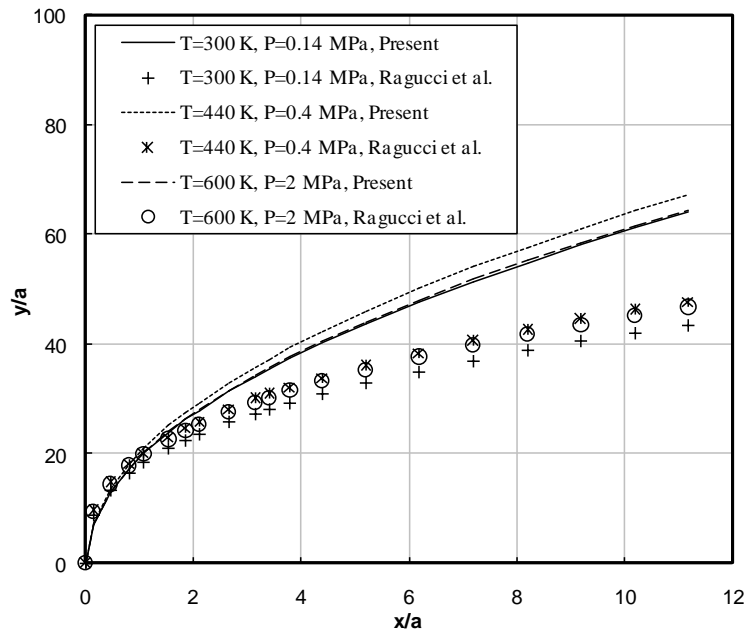


Figure 4-9: Penetration depth of a water jet in crossflow at elevated pressures and temperatures for momentum ratio of 50 compared to experiments of Ragucci *et al.* [30].

In figure 4-9 three different pressures and temperatures are chosen from experiments of Ragucci *et al.* [30]. In the first case (i.e. $T=300$ K, $p=0.14$ MPa) the gas density is low and *Weber* number is equal to 70. In case two (i.e. $T=440$ K, $p=0.4$ MPa), the *Weber* number is 36.3 and the gas velocity is lower because the air density is almost doubled although surface tension between air and water is lowered to 0.042 N/m (calculated at free stream and liquid average temperature). This results in a reduction of drag force and enhancement of penetration. In the third case, the air density is increased almost seven times and its viscosity has also increased. Since the *Weber* number is about 40, the drag coefficient is larger than that of case two and the jet trajectory is lowered. Overall, the penetration depths are overpredicted by the present model. It should be noted that the correlation of Ragucci *et al.* [30] is a weak function of We_{aero} and strongly depends on air viscosity (with power index of 0.186), which clearly explains why increasing the temperature, increases the penetration depth regardless of changing the *Weber* number.

All the results presented in previous sections belong to circular jets, since to date related experimental data is not available for liquid elliptical jets injected into gaseous crossflow. One of the main objectives of this thesis is developing a correlation to predict the trajectories of elliptical jets. In this regard, equations (1-15) to (1-17) are used to calculate the drag coefficients for circular jets and elliptical jets with aspect ratios greater than one. The drag coefficients for aspect ratios of 0.5 and 0.25 are obtained from 2-D analysis presented in §4.1. Thus, equations (4-10) and (4-11) are employed to calculate the drag coefficients for aspect ratios of 0.5 and 0.25, respectively. The results for various aspect ratios at momentum ratios of 100, 50, and 10 are illustrated in figure 4-10. It is inferred from the results that the penetration depth is reduced for all the momentum ratios as the aspect ratio of the jet increases. This behavior can be explained from the aerodynamic point of view; for instance, when the momentum ratio is equal to 10 the drag coefficients for aspect ratios of 4 and 0.25 are equal to 1.47 and 0.29, respectively. Increasing the aspect ratio of the elliptical jet for the same momentum ratio increases the frontal area of the liquid column exposed to the crossflow. Hence, the drag force exerted on the jet is increased and the penetration depth is reduced.

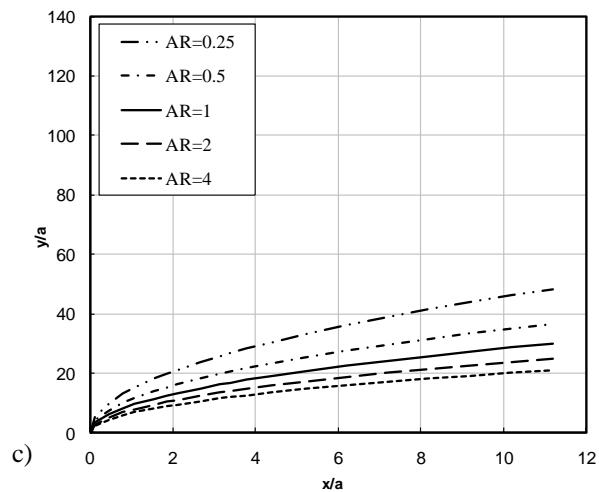
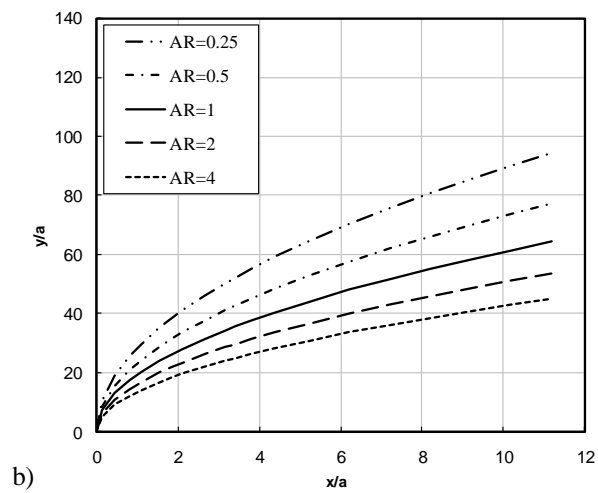
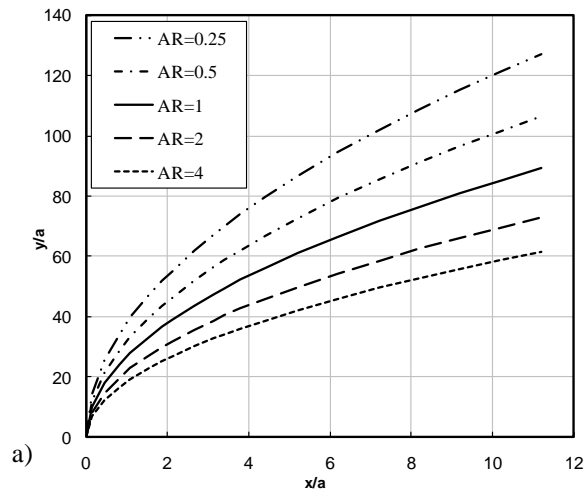


Figure 4-10: Trajectories of elliptical jets with various aspect ratios for momentum ratios of (a) 100, (b) 50, and (c) 10.

4.3 3-D numerical results

The jet in crossflow is inherently a 3-D phenomenon, thus, a 2-D model is not capable of capturing all the features of such a complex flow. Therefore, a circular jet with a diameter of 1 mm with an average velocity of 2.7 m/s injected into the gas stream is modeled. The crossflow velocity is varied to obtain three momentum ratios of 10, 50, and 100 for simulations. Hence, the freestream *Weber* number varies for different momentum ratios. The simulations start with zero gas velocity, i.e. the liquid jet is injected to quiescent air. Then, the crossflow is introduced with a uniform velocity profile. Figure 4-11 illustrates the side-view profiles of a circular jet injected to gas flows at three momentum ratios.

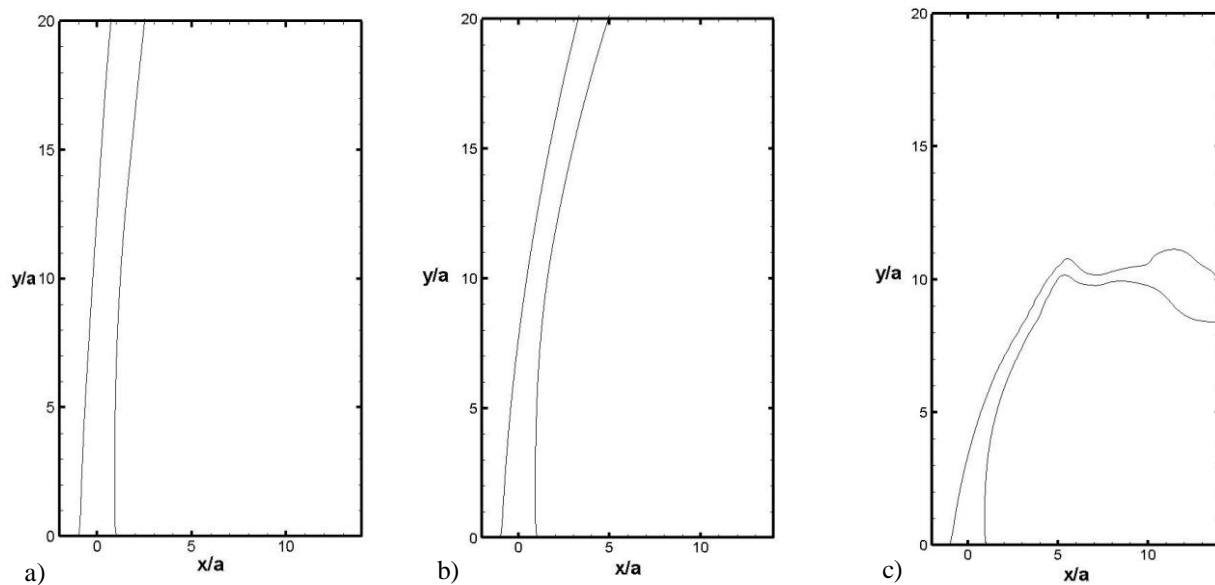


Figure 4-11: Liquid jet profiles for momentum ratios of (a) 100, (b) 50, and (c) 10.

The freestream *Weber* number is equal to one for momentum ratio of 100, therefore, the jet column is slightly deformed. By increasing the *Weber* number to two at momentum ratio of 50,

the jet deformation is enhanced. In figure 4-11-c, where both the *Weber* number and momentum ratio are equal to 10, the jet penetration is reduced and its profile is narrowed due to the gas flow. To illustrate the influence of the freestream, the cross-sections of the jets presented in figure 4-11 are plotted at various vertical distances from the jet exit as it penetrates to the crossflow and presented in figure 4-12.

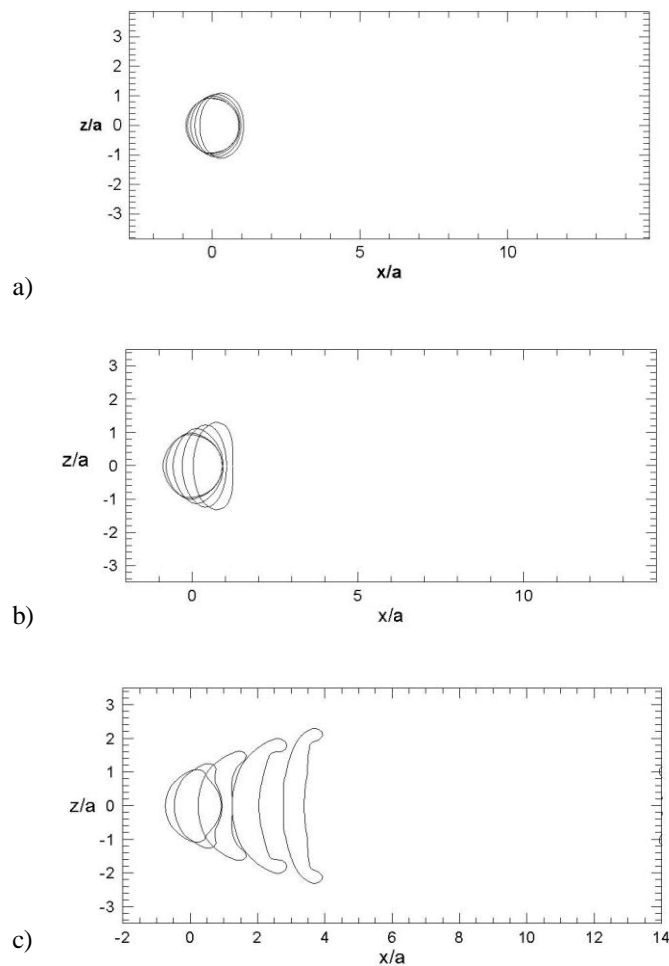


Figure 4-12: Liquid jet cross-sections for momentum ratios of (a) 100, (b) 50, and (c) 10.

In general, the cross-section of the jet is deformed because of the pressure distribution around the jet as illustrated in figure 4-12 for a momentum ratio of 100. The pressure coefficient is the

highest at the stagnation point ($\beta=0$) and drops rapidly until the separation angle. Then, the pressure increases in the wake region and reaches a plateau after 90 degrees. Therefore, the jet radius is elongated perpendicular to the crossflow from the edges where the pressure is lower and contracted in the freestream direction. It can be seen that the variations in the jet aspect ratio are small at very low *Weber* number. As the *Weber* number is increased, it is noticeable that the circular section is deformed to an elliptical shape followed by an increase in the major axis of the ellipse normal to the crossflow. At *Weber* number equal to 10 shown in figure 4-12-c, the jet is stretched from the edges and a kidney shape is formed as it emerges and penetrates to the gas stream. It can be seen that the jet section is almost flattened prior to the breakup.

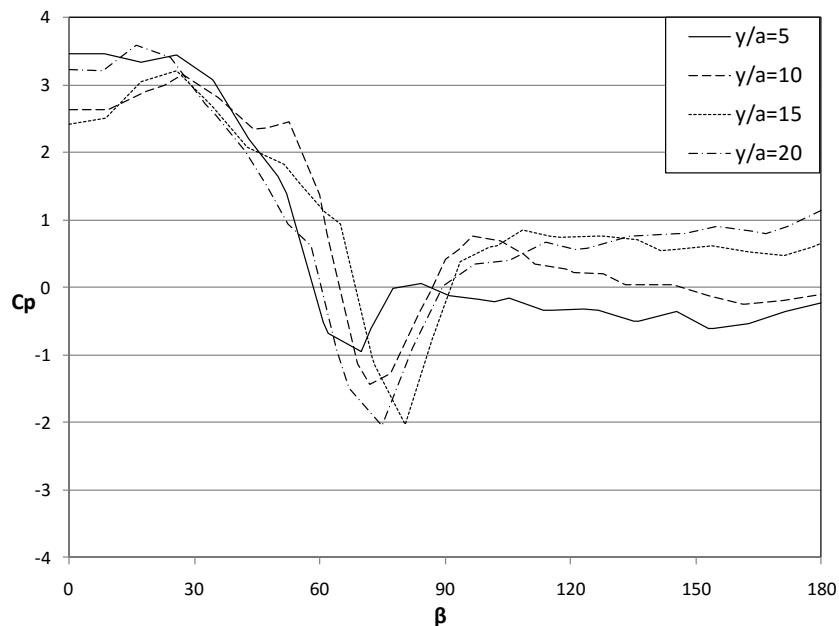


Figure 4-13: Pressure coefficient on the half-jet perimeter at four elevations for momentum ratio of 100.

The near-field trajectories of the circular jet discussed above are compared against the analytical correlation developed in this work and experimental data of Wu *et al.* [26]. The penetration depths in the numerical part are calculated up to 30 jet radii due to limitations in computational resource. The results are presented in figure 4-14 for three momentum ratios of 100, 50, and 10. Overall, the numerical model underpredicts the penetration depths compared to the theoretical model and experimental results. It is speculated to be due to the shortcomings in modeling turbulence since *RANS* models are generally overdissipative. This can be explained by comparison with a flow past a blunt body in transition regime. The drag coefficient drops rapidly after the critical *Reynolds* number for circular and elliptical cylinders in a freestream flow. Therefore, if the turbulent eddies are damped by the turbulence model, the transition from laminar to turbulent flow is delayed. Since the drag coefficient is higher in the laminar regime compared to the transition regime the drag force exerted on the jet is overpredicted by the model, hence, a lower trajectory is observed.

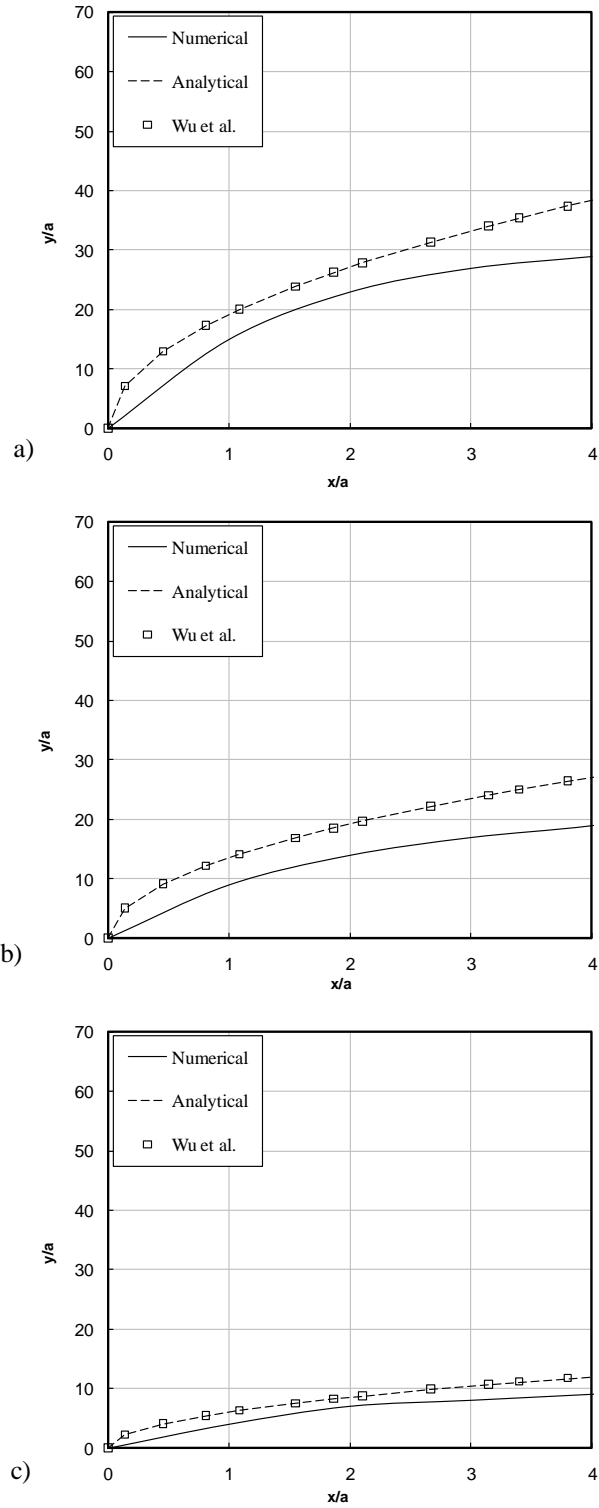


Figure 4-14: Trajectories of a circular jet at momentum ratios of (a) 100, (b) 50, and (c) 10.

The dimensionless axial velocity contours for momentum ratios of 100, 50, and 10 are presented in figures 4-15, 4-16, and 4-17, respectively. In all the cases the solid lines represent the jet interface and three vertical distances are chosen. It is observed that the gas accelerates around the jet and two maxima appear at the edges of the jet cross-section. Downstream of the jet a backflow is developed as the result of the negative pressure gradient in the wake region and it grows in spanwise direction as the jet frontal area is increased. The relation between the aspect ratio of the jet as it penetrates into the crossflow and the width of the wake growth is conspicuous for all the momentum ratios. As the momentum ratio decreases, i.e. the freestream velocity increases since the jet is injected with a constant velocity, the cross-section elongation is enhanced. The jet is deformed to almost a sheet at 8 jet radii as shown in figure 4-17-c. The drag force exerted on the jet is enhanced by increasing the crossflow velocity since the pressure distribution around the jet is altered. The pressure is increased at the stagnation point on the jet and decreased behind the jet. Hence, the pressure drag is increased as a result. This augmentation in drag force causes further elongation of the cross-section as the liquid jet is easily deformable. This deformation continues until the jet breaks up eventually.

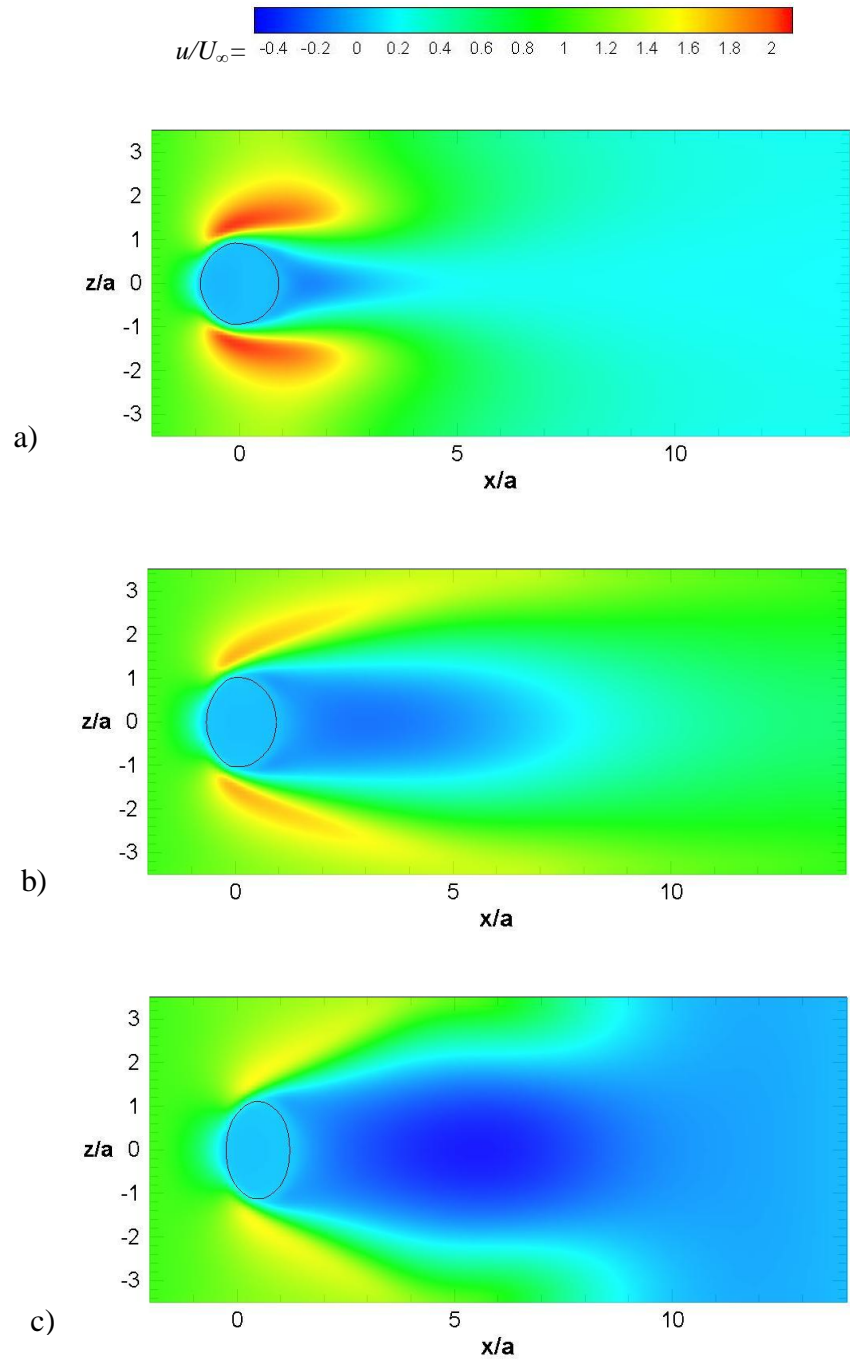


Figure 4-15: Contour of streamwise velocity for momentum ratio of 100 at (y/a): (a) 1, (b) 5, and (c) 10.

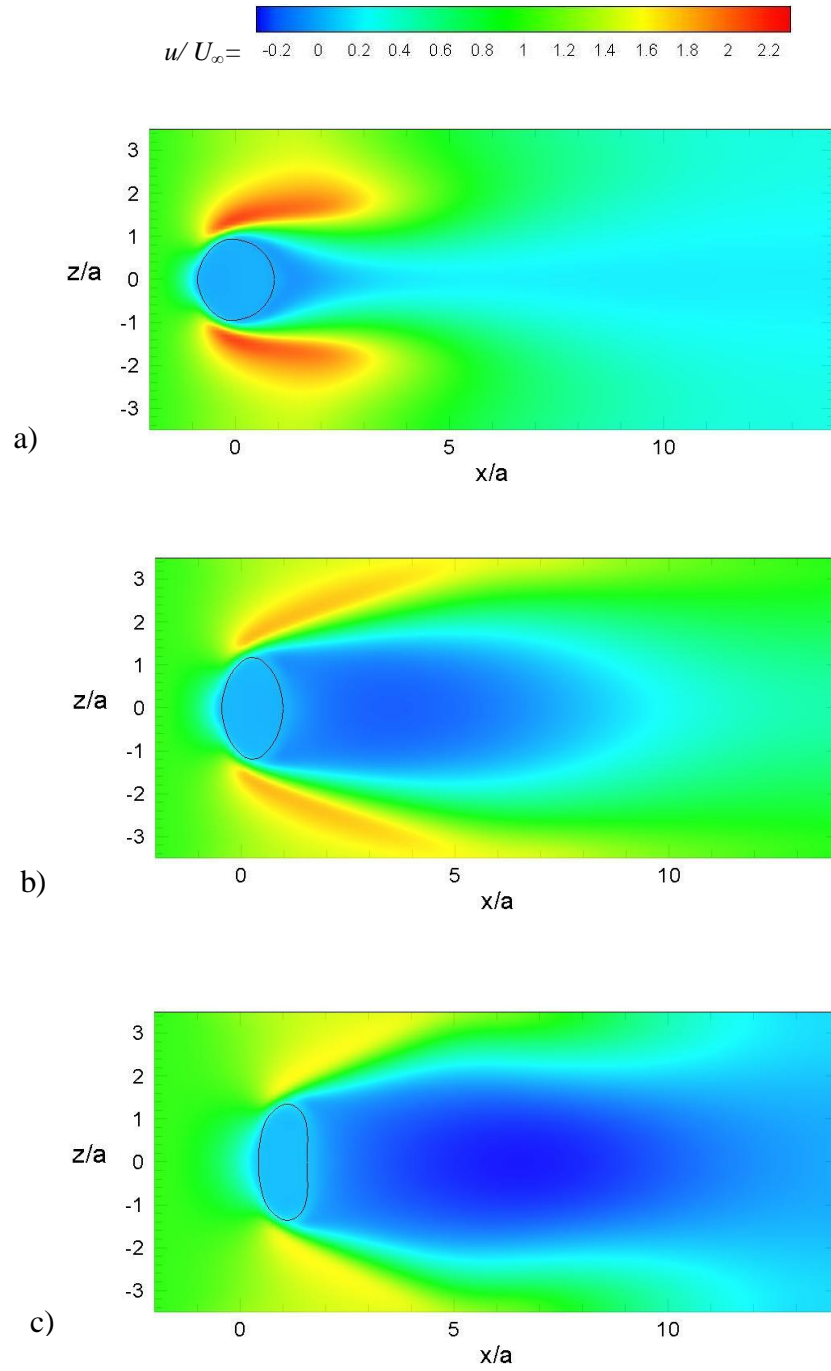


Figure 4-16: Contour of streamwise velocity for momentum ratio of 100 at (y/a) : (a) 1, (b) 5, and (c) 10.

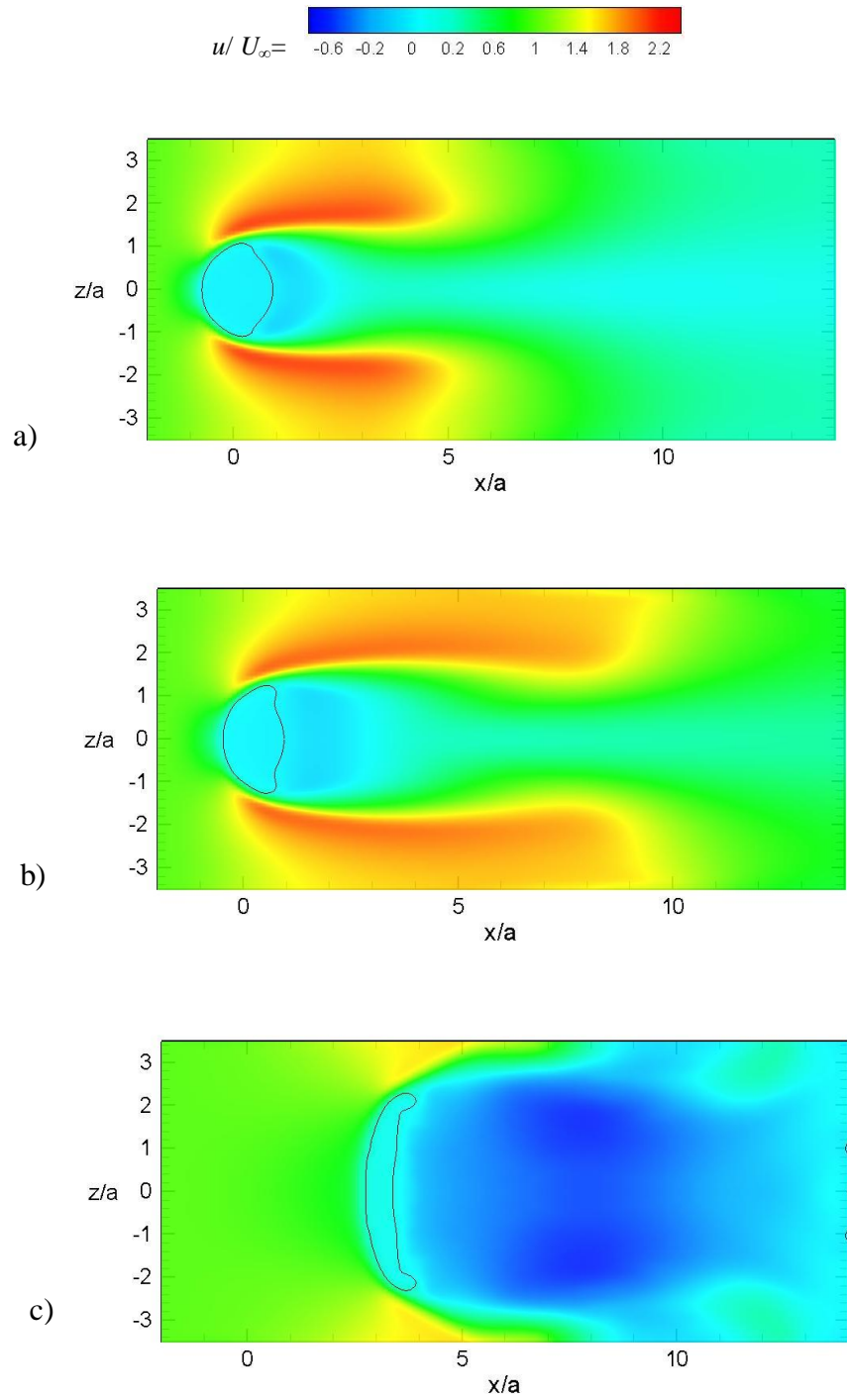


Figure 4-17: Contour of streamwise velocity for momentum ratio of 10 at (y/a): (a) 1, (b) 2, and (c) 8.

The dimensionless vertical velocity is plotted for momentum ratios of 100, 50, and 10 in figures 4-18, 4-19, and 4-20, respectively. The liquid jet cross-section and the contours are shown at three elevations from the jet exit. The jet is injected with a parabolic velocity profile from the inlet; hence, the velocity is twice the average velocity V_j at the jet center. At y/a greater than one, the vertical velocity is close to V_j inside the solid line representing the jet boundary. The velocity is slightly lower in the gas phase near the jet interface because of the shear stress induced by the jet motion. Negative velocities are noticeable behind the jet as the gas flow is disturbed by the velocity gradient as a result of interaction between the two phases. Further downstream the reverse flow region grows in size and is carried away from the jet.

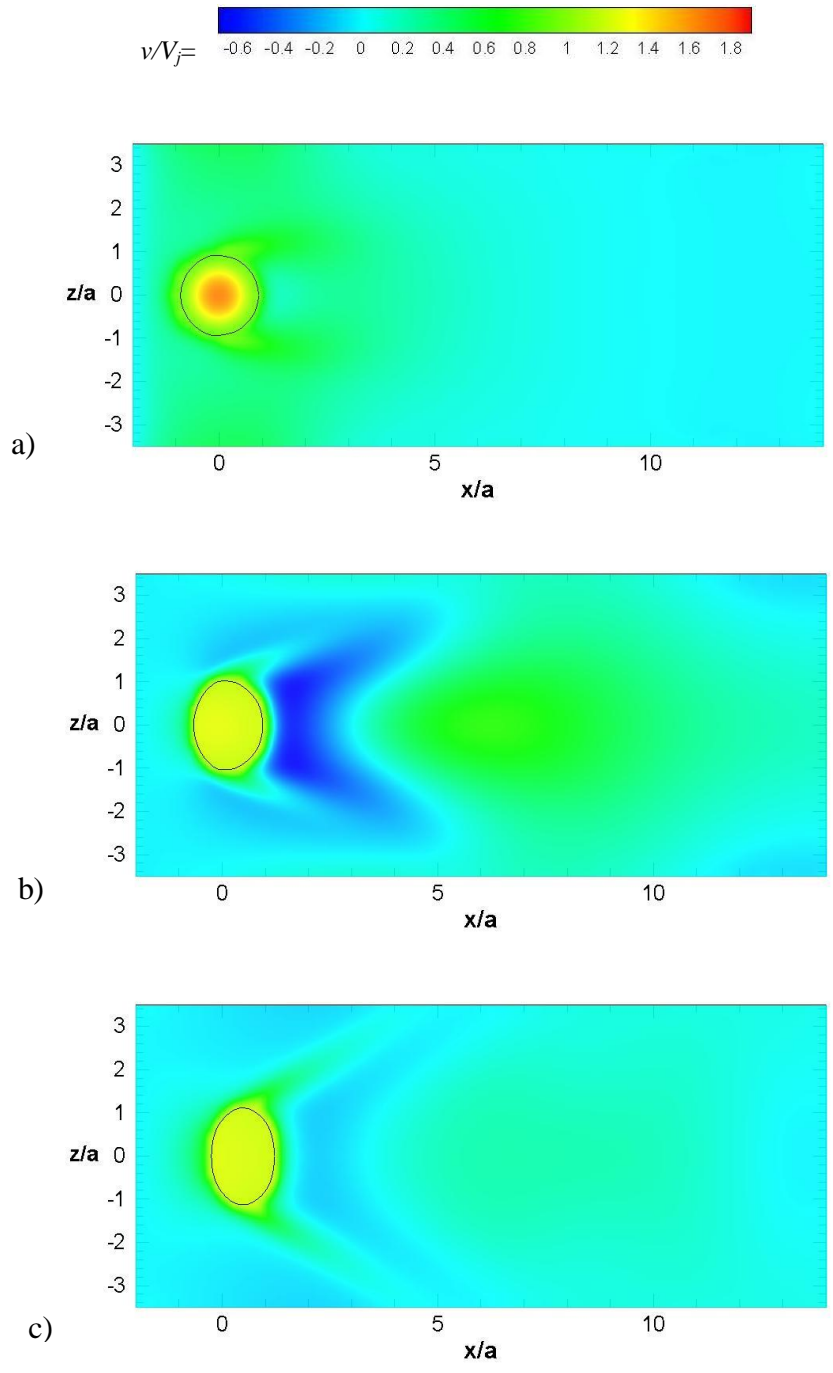


Figure 4-18: Contours of vertical velocity for momentum ratio of 100 at (y/a): (a) 1, (b) 5, and (c) 10.

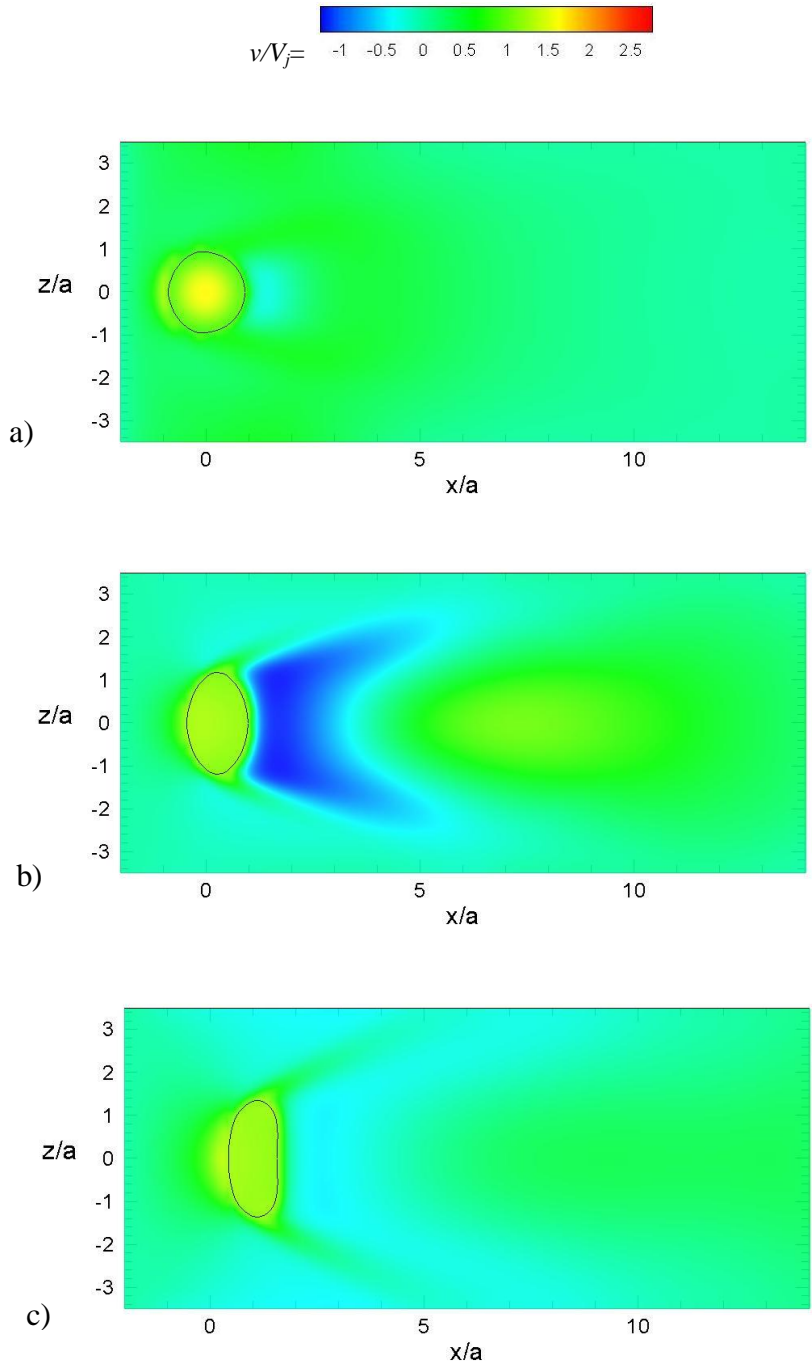


Figure 4-19: Contours of vertical velocity for momentum ratio of 50 at (y/a): (a) 1, (b) 5, and (c) 10.

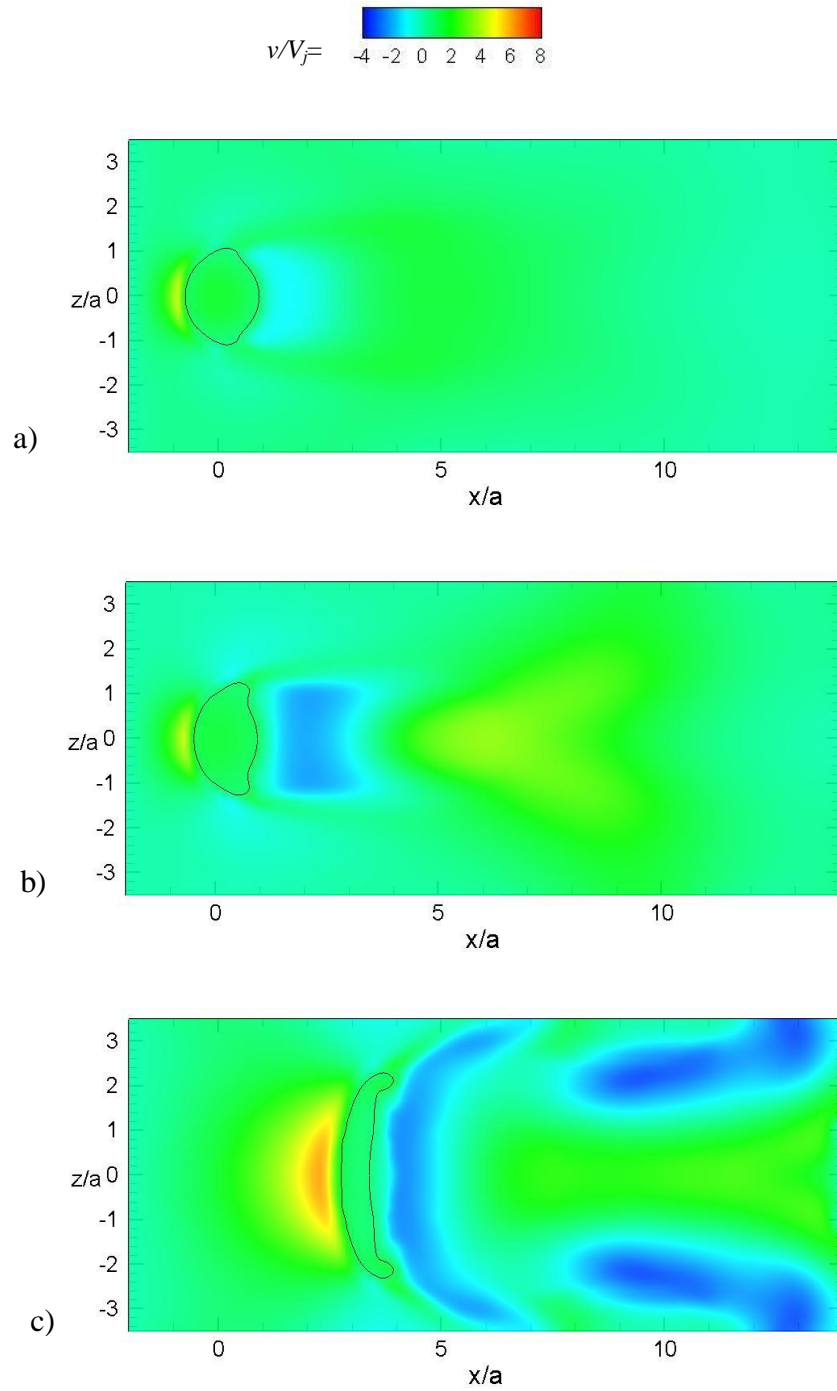


Figure 4-20: Contours of vertical velocity for momentum ratio of 10 at (y/a): (a) 1, (b) 2, and (c) 8.

The contours of dimensionless turbulent kinetic energy are presented for momentum ratios of 100, 50, and 10 in figures 4-21, 4-22, and 4-23, respectively. It should be mentioned that the turbulent kinetic energy is nondimensionalized with respect to the freestream velocity. A highly turbulent region is noticeable at the wind side and edges of the jet. This envelope of turbulent flow moves with the jet in streamwise direction as the jet penetrates into the crossflow. On the other hand, a less turbulent region is observed in the wake of the jet for all three cases, and inside the jet boundary the level of turbulent kinetic energy is very low. It can be seen that the turbulent strips (shown by green color) that shed from the edges of the liquid jet become narrower when the momentum ratio is reduced. Conversely, the size of the region where the turbulence is less concentrated grows as the jet cross-section is flattened by the crossflow at lower momentum ratios.

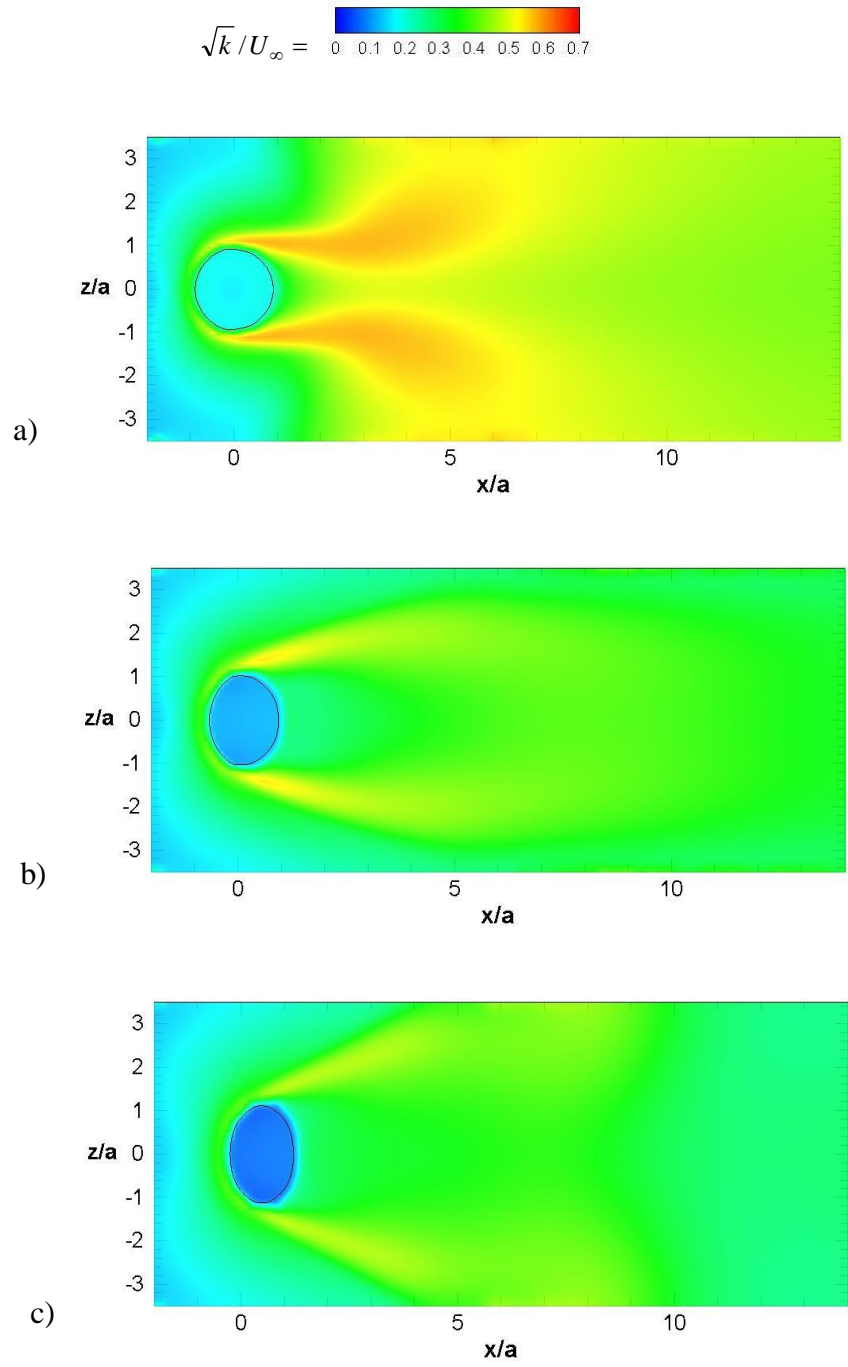


Figure 4-21: Contours of turbulent kinetic energy for momentum ratio of 100 at (y/a): (a) 1, (b) 5, and (c) 10.

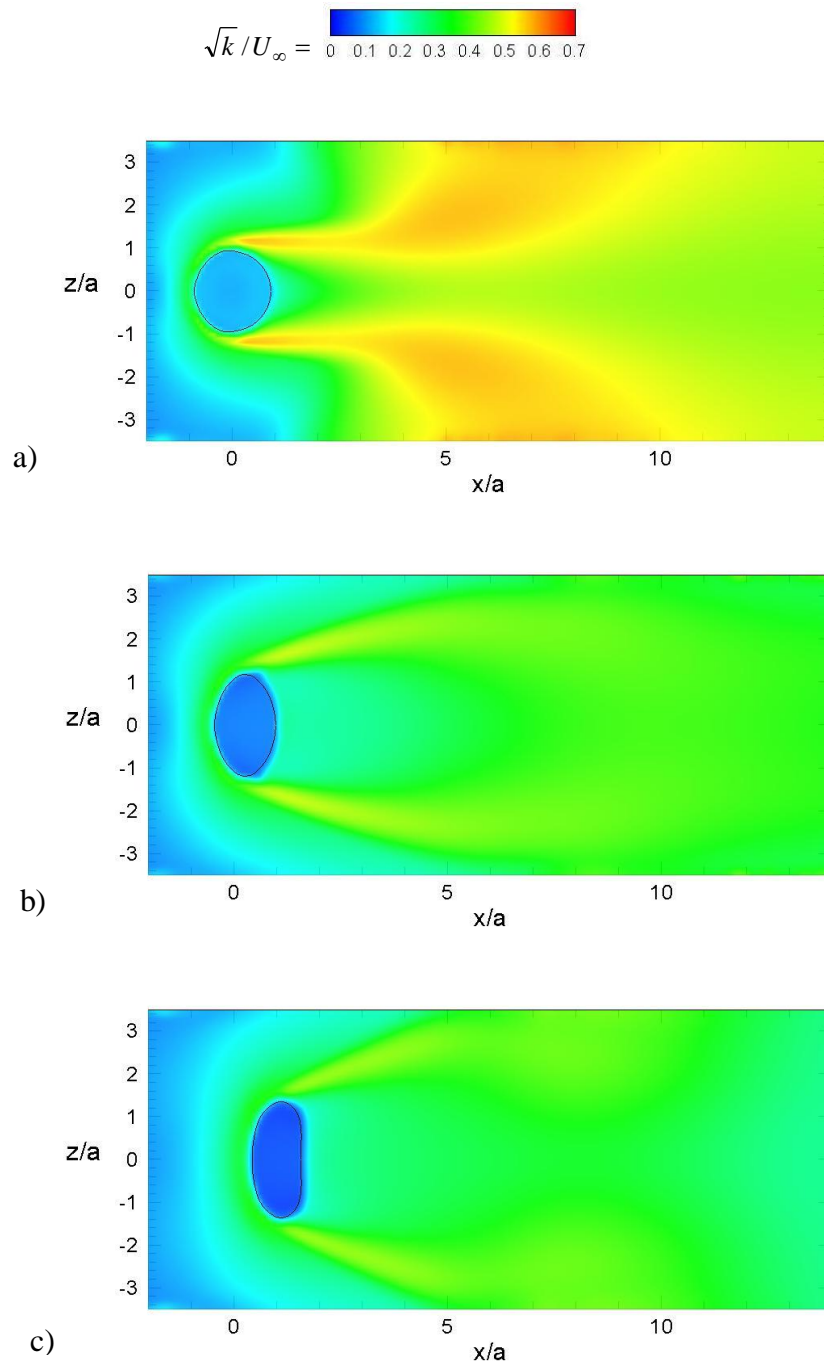


Figure 4-22: Contours of turbulent kinetic energy for momentum ratio of 50 at (y/a): (a) 1, (b) 5, and (c) 10.

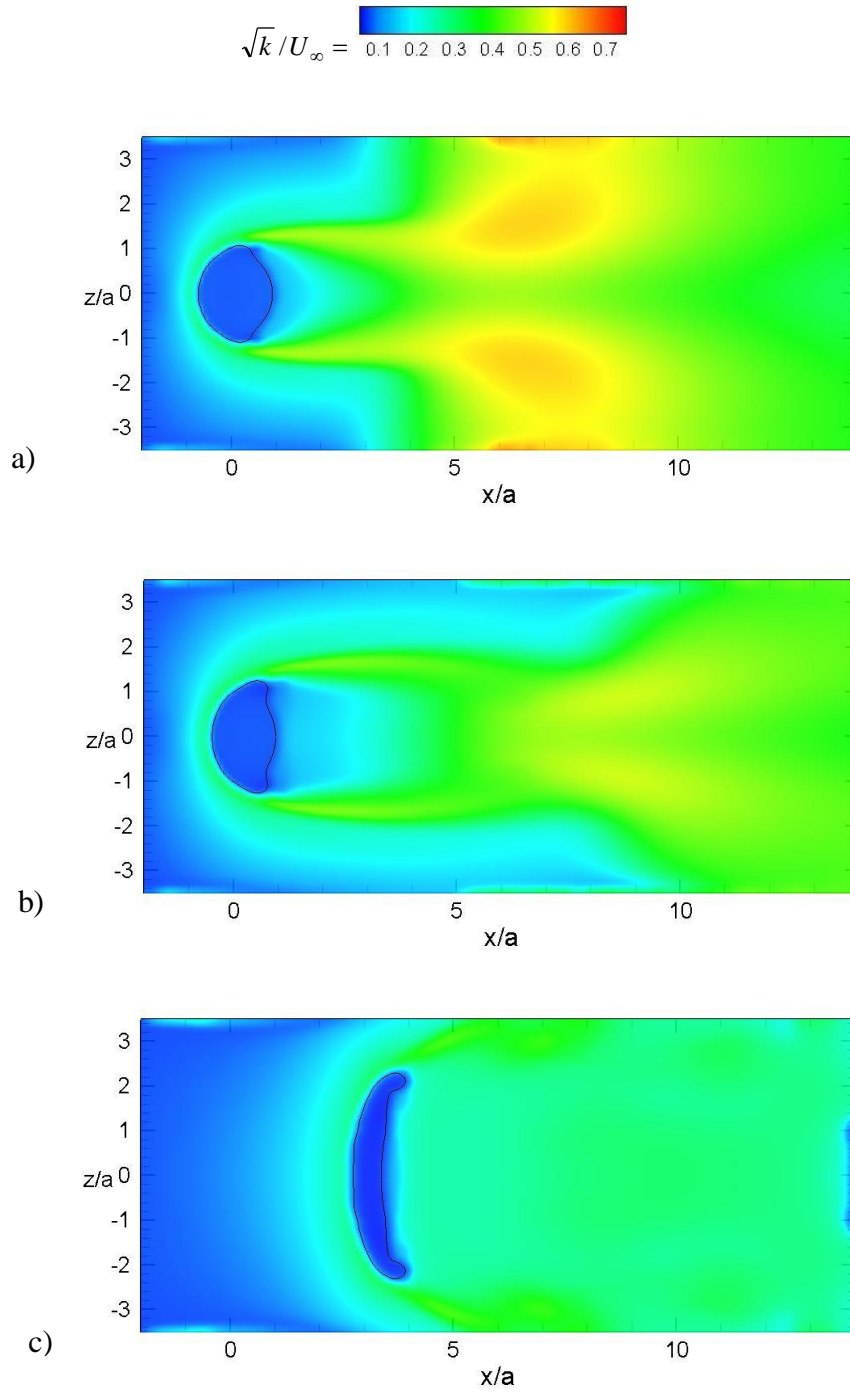
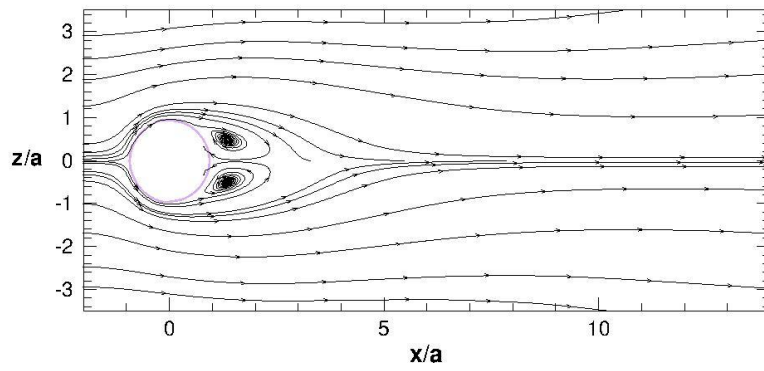
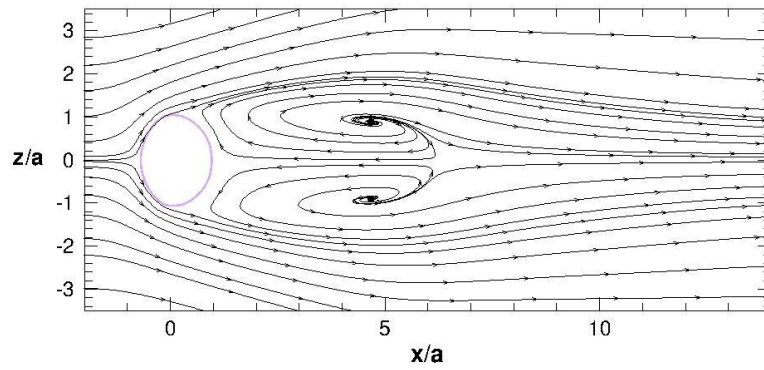


Figure 4-23: Contours of turbulent kinetic energy for momentum ratio of 10 at (y/a): (a) 1, (b) 2, and (c) 8.

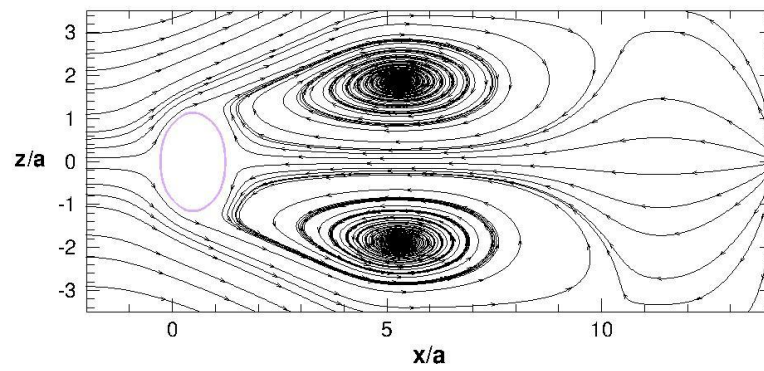
The gas streamlines are plotted for momentum ratios of 100, 50, and 10 in figures 4-24, 4-25, and 4-26, respectively. The flow is laminar for the momentum ratio equal to 100 since the freestream *Reynolds* number is 540. It should be mentioned that the jet initial diameter is used as the characteristic length to calculate the *Reynolds* number. A laminar separation of the flow is noticeable right behind the jet giving rise to the formation of a vortex pair which grows in size at higher elevation. The streamlines at y/a equal to 10 clearly indicate the size of the counter-rotating vortex pair at the lee side of the jet. In figure 4-25, the momentum ratio is equal to 50 and the gas *Reynolds* number is increased to 765. The separation occurs almost at 90 degrees from the stagnation point of the jet and the size of the vortex pair has increased compared to the momentum ratio of 100. The wake region behind the jet also becomes larger as the aspect ratio of the jet is increased. For the momentum ratio equal to 10, shown in figure 4-26, the freestream *Reynolds* number is about 1200 and a large recirculation of the gas flow is observed in the wake of the jet. However, the counter-rotating vortex pair does not appear until y/a equal to 8. Since the drag force exerted on the jet is higher at this momentum ratio, the jet deformation is increased and the cross-section is stretched from the edges. At this momentum ratio the jet cross-section is no longer elliptical and a kidney-like deformation is noticeable. As the jet penetrates into the crossflow the jet elongation continues and the cross-section is flattened at higher elevations.



a)

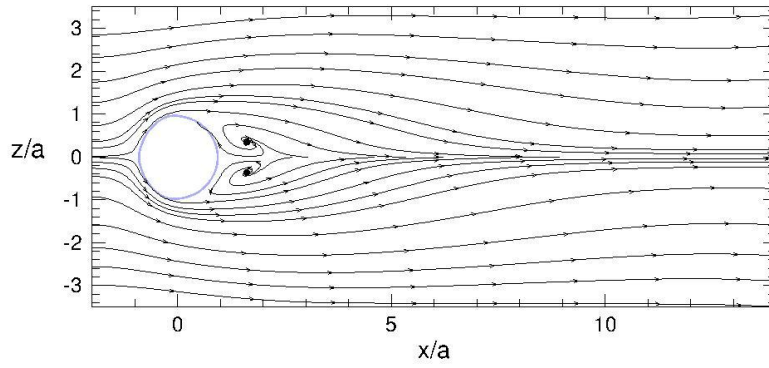


b)

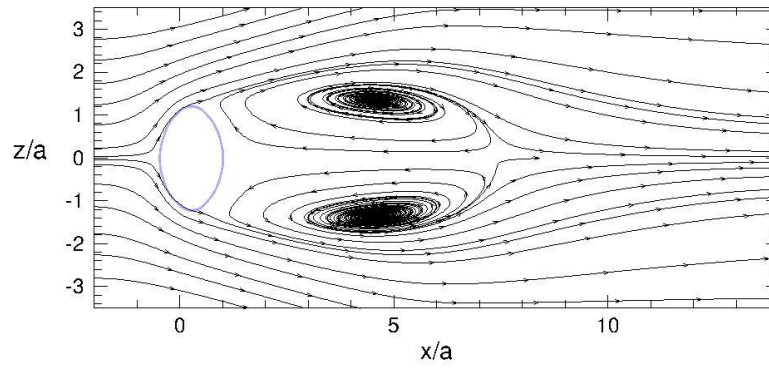


c)

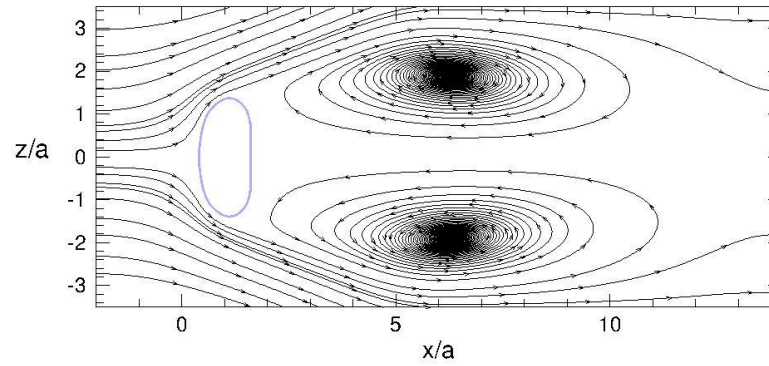
Figure 4-24: Streamlines for momentum ratio of 100 at (y/a) : (a) 1, (b) 5, and (c) 10.



a)



b)



c)

Figure 4-25: Streamlines for momentum ratio of 50 at (y/a): (a) 1, (b) 5, and (c) 10.

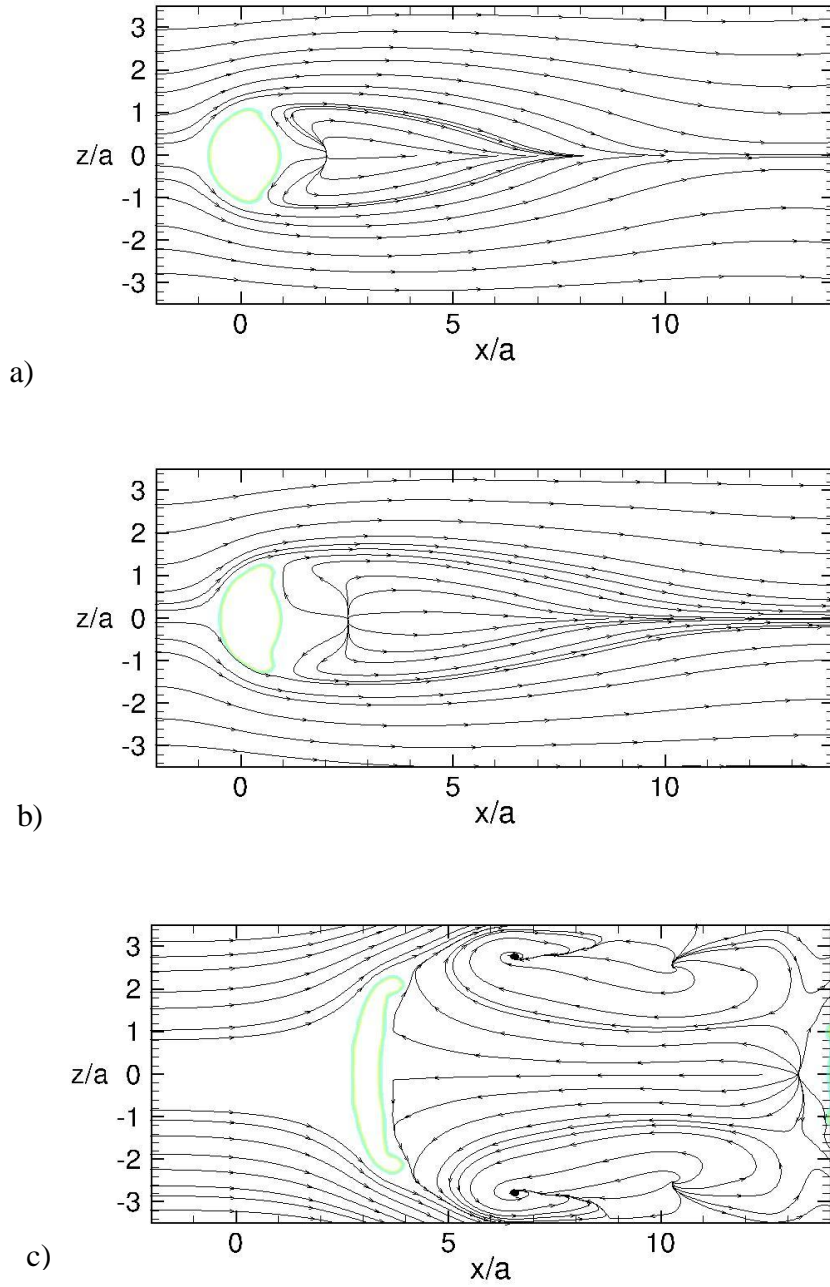


Figure 4-26: Streamlines for momentum ratio of 10 at (y/a): (a) 1, (b) 2, and (c) 8.

5 Closure

5.1 Conclusions

A theoretical analysis of liquid jets in a subsonic crossflow was carried out. An analytical correlation for the jet trajectory was developed and the results were compared against experimental data available in the literature. It was shown that the drag coefficient can significantly affect the results. Although the viscous force was not included in this model, the changes in liquid viscosity were considered in terms of the drag coefficient calculated from equation (1-7). The results illustrated that the trend of changes in liquid density is followed, even though in some cases the penetration depths were overpredicted. At elevated pressure and temperature, the jet penetration was overpredicted by the present correlation compared to experiments. This could be due to the fact that the liquid evaporation and mass stripping from the jet surface become more important when the freestream temperature and pressure are increased. In addition, the empirical correlations use directly the gas properties in calculating *Weber* or *Reynolds* numbers, whereas in the present model the changes in gas properties are incorporated in terms of the drag coefficient. Hence, present correlation seems to be more promising at ambient pressure and temperature.

In the numerical part, the drag coefficients for elliptical jets with aspect ratios of 0.5 and 0.25 were calculated based on a 2-D model. The two correlations found based on freestream *Reynolds* number from 2-D analysis were employed in calculating the trajectories of elliptic jets. The results revealed that the jets with lower aspect ratios penetrate more into the crossflow since they have lower drag coefficients.

A 3-D model was generated for the simulations since a 2-D model cannot capture the deformation of the jet cross-section. A circular jet injected into gas crossflows at momentum ratios of 10, 50, and 100 was simulated. It was inferred from the results that the jet deformation was directly influenced by the freestream *Weber* number. As the *Weber* number was increased, the jet elongated normal to the crossflow direction. The jet cross-section was deformed to an ellipse first, followed by kidney-shape formation and at high *Weber* numbers the jet was flattened prior to the breakup. The changes in the aspect ratio can be explained by the drag force exerted on the jet as the pressure distribution around the jet is altered. The higher pressure at the stagnation point on the jet causes contraction in the direction of the crossflow.

The contours illustrated that the size of the wake region behind the jet is governed by the aspect ratio of the jet cross-section. Moreover, a highly turbulent flow was observed on the wind side and at the edges of the jet. This turbulent region was convected downstream by the crossflow. The width of the strips around the jet where high concentration of the turbulence is observed was contracted by increasing the freestream *Weber* number.

The gas streamlines around the jet revealed the formation of a *Counter-rotating Vortex Pair (CVP)* which is one of the main features of liquid jet penetration into a gaseous crossflow. Furthermore, the size of the vortex pair was increased when the momentum ratio was reduced and the laminar separation occurred sooner on the jet. Hence, the size of the wake region behind the jet was increased by reducing the momentum ratio.

5.2 Recommendations for future work

- The 3-D simulations in the present work were limited to circular jets in the crossflow. Therefore, modeling of elliptical jets with various aspect ratios would be the next step. This way a one-to-one comparison between the analytical correlation developed in this work and the numerical results for elliptic jets will be accomplished.
- The injection angle of the jet is of importance as it will affect the penetration depth in the crossflow. This can be achieved by modifying the theoretical methodology and the numerical model.
- In the numerical model, a fully developed pipe flow with a parabolic velocity profile was assumed for the liquid jet. This assumption holds true for the pipes with sufficient length. However, if the length to diameter ratio of the orifice is not large enough a plug flow is expected. The effect of the liquid velocity profile at the injection point can be numerically studied as an extension of this work.
- The current turbulence model has shown some shortcomings in modeling liquid jet in gaseous crossflow. Therefore, *Large Eddy Simulation (LES)* and *Direct Numerical Simulation (DNS)* are proposed to model turbulence in future studies.
- The present work focused on the near-field trajectory of the jet where a liquid core is observed. To calculate the size of the droplets produced by the jet breakup, a hybrid model is required. The primary breakup of the jet can be captured by *Volume of Fluid* method. Then, a discrete phase model is needed to track the produced droplets in a Lagrangian frame. Moreover, at high *Weber* numbers the surface breakup mode is dominant. Hence, very fine grid resolution is needed to capture the small droplets sheared off the jet surface.

6 Bibliography

1. *Flow and breakup characteristics of elliptical liquid jets.* **Kasyap, T. V., Sivakumar, D. and Raghunandan, B. N.** s.l. : International Journal of Multiphase Flow, 2009, Vol. 35, pp. 8–19.
2. *Atomization and Sprays.* **Lefebvre, Arthur H.** s.l. : Combustion: An International Series, 1989, Combustion: An International Series.
3. *Mechanisms of breakup of round liquid jets.* **Reitz, R. D. and Bracco, F. V.** [ed.] N Cheremisnoff. Houston: Gulf : The Encyclopedia of Fluid Mechanics, 1986, Vol. 3, pp. 233–49.
4. *Mechanism of Disintegration of Liquid Sheets.* **York, J. L., Stubbs, H. E. and Tek, M. R.** s.l. : Transactions of ASME, 1953, Trans. ASME, Vol. 75, pp. 1279-1286.
5. *Mechanism of Atomization of a Liquid Jet.* **Bracco, F. V. and Reitz, R. D.** 2, 1982, Physics of Fluids, Vol. 25, pp. 1730-1741.
6. *Fundamental Classification of Atomization Processes.* **Lightfoot, M. D. A.** 11, s.l. : Atomization and Sprays, 2009, Atomization and Sprays, Vol. 19, pp. 1065-1104.
7. *On the instability of jets.* **Rayleigh, L.** s.l. : London Mathematical Society Monographs, 10, 1879.
8. *Disintegration of liquid jets.* **Weber, C.** 2, s.l. : Zeitschrift für Angewandte Mathematik und Mechanik, 1931, Vol. 11, pp. 136-159.
9. *Generation of ripples by wind blowing over viscous fluids.* **Taylor, G. I.** [ed.] G. K. Batchelor. s.l. : Cambridge University Press, Cambridge, UK, 1962, The scientific Papers of G. I. Taylor, Vol. 3, pp. 244–254.
10. *Atomization and other Breakup Regimes of a Liquid Jet.* **Reitz, R. D.** s.l. : PhD. Thesis, Princeton University, 1978.

11. *Correlation of experimental data on the disintegration of liquid jets.* **Miesse, C. C.** s.l. : Industrial Engineering Chemistry, 1955, Vol. 47, pp. 1690–1695.
12. *Formation of Drops by Nozzles and Breakup of Liquid Jets.* **Ohnesorge, W.** s.l. : Zeitschrift für Angewandte Mathematik und Mechanik , 1936, Vol. 16, p. 355.
13. *Drop and Spray Formation from a Liquid Jet.* **Lin, S. P. and Reitz, R. D.** s.l. : Annual Review of Fluid Mechanics, 1998, Vol. 30, pp. 85–105.
14. *Energy budget in atomization.* **Lin, S. P. and Creighton, B.** s.l. : Aerosol Science and Technology, 1990, Vol. 12, pp. 630–636.
15. *On the experimental investigation on primary atomization of liquid streams.* **Dumouche, C.** s.l. : Experiments in Fluids, 2008, Vol. 45, pp. 371–422.
16. *On sprays and spraying.* **Ranz, W. E.** Penn State Univ. : A survey of spray technology for research and development engineers, 1956.
17. *The instability of capillary jets.* **Sterling, A. M. and Sleicher, C. A.** s.l. : Journal of Fluid Mechanics, 1975, Vol. 68, pp. 477–495.
18. *Modeling Engine Spray and Combustion Processes.* **Stiesch, G.** s.l. : Springer, 2003.
19. *Newtonian Jet Stability.* **Grant, R. P. and Middlemann, S.** s.l. : AIChE Journal, 1966.
20. *A review on Penetration Heights of Transverse Liquid Jets in High Speed Flows.* **Lin, K. C., Kennedy, P. J. and Jackson, T. A.** s.l. : ILASS Americas, 15th Annual Conference, 2007.
21. *Properties of nonturbulent round liquid jets in uniform gaseous crossflows.* **Aalburg, C., et al.** s.l. : Atomization and Spray, 2005, Vol. 15, pp. 271–294.
22. *Ballistic imaging of the liquid core for a steady jet.* **Linne, Mark A., et al.** 31, s.l. : Applied Optics, 2005, Vol. 44.

23. *Primary Breakup of Nonturbulent Round Liquid Jets in Gas Crossflows.* **Mazallon, J., Dai, Z. and Faeth, G. M.** 3, s.l. : Atomization and Sprays, 1999, Vol. 9, pp. 291-312.
24. *Investigation of a Liquid Jet in a Subsonic Cross-flow.* **Vich, G. and Ledoux, M.** 1-3, s.l. : International Journal of Fluid Mechanics Research, 1997, Vol. 24.
25. *Spray Trajectories of Liquid Fuel Jets in Subsonic Crossflows.* **Wu, P. K., et al.** 1-3, s.l. : International Journal of Fluid Mechanics Research, 1997, Vol. 24.
26. *Breakup Processes of Liquid Jets in Subsonic Crossflows.* **Wu, P. K., et al.** 1, s.l. : Journal of Propulsion and Power, 1997, Vol. 13.
27. *Breakup and Atomization of Kerosene Jet in Crossflow at Elevated Pressure.* **Hassa, C. and Beckerand, J.** s.l. : Atomization and Sprays, 2002, Vol. 11, pp. 49-67.
28. **Tambe, Samir B.** *Liquid Jets in Subsonic Crossflow.* s.l. : University of Cincinnati, 2004.
29. *Penetration of Liquid Jets in a cross-flow.* **Stenzler, Jacob N., Lee, Jong G. and San, Domenic A.** s.l. : Atomization and Sprays, 2006, Vol. 16, pp. 887-906.
30. *Breakup and breakdown of bent kerosene jets in gas turbine conditions.* **Ragucci, Raffaele, Bellofiore, Alessandro and Cavaliere, Antonio.** s.l. : Proceedings of the Combustion Institute, 2007. Vol. 31, pp. 2231–2238.
31. *Trajectory of a Liquid Jet in High Pressure and High Temperature Subsonic Air Crossflow.* **Amighi, A., Eslamian, M. and Ashgriz, N.** s.l. : ICLASS 2009.
32. *Improved Model for the Penetration of Liquid Jets in Subsonic Crossflows.* **Mashayek, A., Jafari, A. and Ashgriz, N.** 11, s.l. : AIAA JOURNAL, 2008, Vol. 46.
33. *Steady flow of power-law fluids across an unconfined elliptical cylinder.* **Sivakumar, P., Bharti, R. P. and Chhabra, R. P.** s.l. : Chemical Engineering Science 62, 2007, pp. 1682 – 1702.

34. *CFD prediction of the trajectory of a liquid jet in a non-uniform air crossflow.* **Ryan, Matthew J.** s.l. : Computers & fluids, 2006, Vol. 35, pp. 463-476.
35. *Disintegration Phenomena of Metalized Slurry Fuel Jets in High Speed Air Stream.* **Inamura, T., et al.** s.l. : ICLASS-91 Gaithersburg, MD, USA, 1991.
36. *Atomization and Bending of Coherent Deformed Jets in Crossflow.* **Bellofiore, A., et al.** s.l. : Proceedings of the European Combustion Meeting, 2005.
37. *A model for numerical simulation of breakup of a liquid jet in crossflow.* **Madabhushi, Ravi K.** s.l. : Atomization and Sprays, 2003, Vol. 13, pp. 413-424.
38. *Bag breakup of nonturbulent liquid jets in crossflow.* **Ng, C. L., Sankarakrishnan, R. and Sallam, K. A.** s.l. : International Journal of Multiphase Flow, 2008, Vol. 34, pp. 241–259.
39. **Fric, T. F.** *Structure in the near field of the transverse jet.* s.l. : Ph.D. thesis, California Institute of Technology .
40. *Vortical structure in the wake of a transverse jet.* **Fric, T. F. and Roshko, A.** s.l. : Journal of Fluid Mechanics, 1994, Vol. 279, pp. 1-47.
41. *Elliptic jets in cross-flow.* **New, T. H., Lim, T. T. and Luo, S. C.** s.l. : Journal of Fluid Mechanics, 2003, Vol. 494, pp. 119–140.
42. *Evolution of jets emanating from short holes into crossflow.* **Karagozian, A., Peterson, S. D. and Plesniak, M. W.** s.l. : Journal of Fluid Mechanics, 2004, Vol. 503, pp. 57–91.
43. *The Generation and Decay of Vorticity.* **Morton, B. R.** s.l. : Geophysical and Astrophysical Fluid Dynamics, 1984, Vol. 28, pp. 277-308.
44. *Predictions of Momentum and Scalar Fields in a Jet in Cross-Flow using First and Second Order Turbulence Closures.* **Alvarez, J., Jones, W. P. and Seoud, R.** s.l. : AGARD Meeting on Computational and Experimental Assessment of Jets in Cross Flow, 1993.

45. *Modeling of jets in cross flow with LES-Part 1: Momentum transport for low R w/RANS.* **Dai, Z., Hsieh, S. H. and Mongia, H. C.** Reno, Nevada : AIAA Aerospace Sciences meeting and exhibit, 2005.
46. *Multigrid calculations of a jet in cross flow.* **Vanka, S. P. and Claus, R. W.** Reno, Nevada : AIAA Paper 90-0444, Aerospace Sciences Meeting, 1990.
47. *Fluid flow of a row of jets in crossflow- a numerical study.* **Kim, W. and Benson, S. W.** s.l. : Aerospace Sciences Meeting and Exhibit, 30th, Reno, NV, 1992.
48. *Experimental study of a plume in a crossflow.* **Savory, E., Toy, N. and Ahmed, S.** s.l. : Journal of Wind Engineering and Industrial Aerodynamics 60, 1996, pp. 195-209.
49. *Predictions of a Film Coolant Jet in Crossflow With Different Turbulence Models.* **Hoda, Asif and Acharya, Sumanta.** s.l. : Transactions of the ASME, 2000, Vol. 122.
50. *The Numerical Computation of Turbulent Flows.* **Lauder, B. E. and Spalding, D. B.** s.l. : Computer Methods Applied Mechanics and Engineering, 1974, Vol. 3, pp. 269–289.
51. *Application of the Energy Dissipation Model of Turbulence to the Calculation of Flow Near a Spinning Disc.* **Lauder, B. E. and Sharma, B. I.** s.l. : Letters in Heat and Mass Transfer, 1974, Vol. 1, pp. 131–138.
52. *Modified Form of the Model for Predicting Wall Turbulence.* **Lam, C. K. and Bremhorst, K A.** s.l. : ASME Journal of Fluids Engineering, 1981, Vol. 103, pp. 456–460.
53. *A Complete Model of Turbulence.* **Wilcox, D. C., and Traci, R. M.** s.l. : AIAA Paper No. 76–351, 1976.
54. *Low Reynolds Number Modeling With the Aid of Direct Simulation Data.* **Rodi, W., and Mansour, N. N.** s.l. : Journal of Fluid Mechanics, 1993, Vol. 250, pp. 509–529.

55. *Prediction of Anisotropy of the Near-Wall Turbulence With an Anisotropic Low-Reynolds-Number Turbulence Model.* **Mayong, H. K. and Kasagi, N.** s.l. : ASME Journal of Fluids Engineering, 1990, Vol. 112, pp. 521–524.
56. *On Nonlinear $k - l$ and Models of Turbulence.* **Speziale, C. G.** s.l. : Journal of Fluid Mechanics, 1987, Vol. 178, pp. 459–475.
57. *Multiple Jets in a Crossflow: Detailed Measurements and Numerical Simulations.* **Ajersch, P., et al.** s.l. : ASME Journal of Turbomachinery, 1997, Vol. 119, pp. 330–342.
58. *Characteristics of three-dimensional turbulent jets in crossflow.* **Demuren, A. O.** 6, s.l. : International Journal of Engineering Science, 1993, Vol. 31, pp. 899-913.
59. *Experimental Investigation of Jets in a Cross Flow.* **Andreopoulos, J. and Rodi, W.** s.l. : Journal of Fluid Mechanics, 1984, Vol. 138, pp. 93-127.
60. *Trajectory of a Liquid Jet Traversing Subsonic Airstreams.* **Inamura, Takao.** 1, s.l. : Journal of Propulsion, 1999, Vol. 16.
61. *A Continuum Method for Modeling Surface Tension.* **Brackbill, J. U., Kothe, D. B. and Zemach, C.** s.l. : Journal of Computational Physics, 1992, Vol. 100, pp. 335-354.
62. *Time-Dependent Multi-Material Flow with Large Fluid Distortion.* **Youngs, D. L.** [ed.] K. W. Morton and M. J. Baines. s.l. : Academic Press, 1982, Numerical Methods for Fluid Dynamics.
63. *Lectures in Mathematical Models of Turbulence.* **Spalding, B. E. Launder and D. B.** s.l. : Academic Press, London, England, 1972.
64. *Introduction to the Renormalization Group Method and Turbulence Modeling.* **Choudhury, D.** s.l. : Fluent Inc. Technical Memorandum TM-107, 1993.

65. *Renormalization Group Analysis of Turbulence: I. Basic Theory*. **Orszag, S. A. and Yakhot,**
V. 1, s.l. : Journal of Scientific Computing, 1986, Vol. 1, pp. 1-51.